Geophysical Journal International

Geophys. J. Int. (2013) **194,** 61–77
Advance Access publication 2013 April 12

doi: 10.1093/gji/ggt099

Glacial isostatic adjustment model with composite 3-D Earth rheology for Fennoscandia

Wouter van der Wal,[1] Auke Barnhoorn,[2] Paolo Stocchi,[3,4] Sofie Gradmann,[5] Patrick Wu,[6] Martyn Drury[7] and Bert Vermeersen[1,3]

[1] *Faculty of Aerospace Engineering, Delft University of Technology, Kluyverweg* 1, 2629 *HS, Delft, The Netherlands. E-mail: W.vanderWal@tudelft.nl*
[2] *Faculty of Civil Engineering and Geosciences, Delft University of Technology, The Netherlands*
[3] *NIOZ Royal Netherlands Institute for Sea Research, Den Burg, Texel, The Netherlands*
[4] *Institute for Marine and Atmospheric Research (IMAU), Utrecht, The Netherlands*
[5] *Geological Survey of Norway (NGU), Trondheim, Norway*
[6] *Department of Geoscience, University of Calgary, Canada*
[7] *Department of Earth Sciences, Utrecht University, The Netherlands*

Accepted 2013 March 11. Received 2013 March 8; in original form 2012 August 10

SUMMARY

Models for glacial isostatic adjustment (GIA) can provide constraints on rheology of the mantle if past ice thickness variations are assumed to be known. The Pleistocene ice loading histories that are used to obtain such constraints are based on an a priori 1-D mantle viscosity profile that assumes a single deformation mechanism for mantle rocks. Such a simplified viscosity profile makes it hard to compare the inferred mantle rheology to inferences from seismology and laboratory experiments. It is unknown what constraints GIA observations can provide on more realistic mantle rheology with an ice history that is not based on an *a priori* mantle viscosity profile. This paper investigates a model for GIA with a new ice history for Fennoscandia that is constrained by palaeoclimate proxies and glacial sediments. Diffusion and dislocation creep flow law data are taken from a compilation of laboratory measurements on olivine. Upper-mantle temperature data sets down to 400 km depth are derived from surface heatflow measurements, a petrochemical model for Fennoscandia and seismic velocity anomalies. Creep parameters below 400 km are taken from an earlier study and are only varying with depth. The olivine grain size and water content (a wet state, or a dry state) are used as free parameters. The solid Earth response is computed with a global spherical 3-D finite-element model for an incompressible, self-gravitating Earth. We compare predictions to sea level data and GPS uplift rates in Fennoscandia. The objective is to see if the mantle rheology and the ice model is consistent with GIA observations. We also test if the inclusion of dislocation creep gives any improvements over predictions with diffusion creep only, and whether the laterally varying temperatures result in an improved fit compared to a widely used 1-D viscosity profile (VM2).

We find that sea level data can be explained with our ice model and with information on mantle rheology from laboratory experiments, heatflow and seismology and a pure olivine rheology above 400 km. Moreover, laterally heterogeneous models provide a significantly better fit to relative sea level data than the VM2 viscosity, for our ice model as well as for the ICE-5G model that is based on the VM2 profile. The new ice model gives different constraints on mantle rheology than the ICE-5G model, indicating a possible bias towards mantle viscosity in the latter or shortcomings in our ice model. Present-day uplift rates for a dry rheology are close to GPS observed uplift rate for certain combinations of grain size and temperature fields. Sea level data show a preference for a wet olivine rheology, but in that case uplift rates are too low for all grain sizes and temperature fields. The difficulty to fit sea level data and uplift rate data simultaneously can not be resolved by varying creep parameters below 400 km. Uncertainties in the flow law and the neglect of other materials in the upper mantle, as well as the neglect of flow in the crust could affect our conclusions.

Key words: Sea level change; Creep and deformation; Dynamics of lithosphere and mantle; Kinematics of crustal and mantle deformation; Rheology: mantle.

1 INTRODUCTION

One important application of glacial isostatic adjustment (GIA) studies is to provide information on the fluid behaviour of the Earth's mantle (e.g. Turcotte & Schubert 2002). The rheological behaviour of the mantle is usually parameterised in terms of layered Newtonian viscosity (e.g. Kaufmann & Lambeck 2002; Peltier 2004). However, large deviations can be expected from this 1-D parametrization. It is known from seismology that significant lateral variations in temperature and composition exist (e.g. Goes *et al.* 2000), which imply large lateral variations in viscosity (Ivins & Sammis 1995). Laboratory experiments show that both diffusion and dislocation creep operate at conditions of the upper mantle (Goetze & Kohlstedt 1973; Karato & Wu 1993; Hirth & Kohlstedt 2003). The transition between diffusion and dislocation creep mechanisms occurs at stresses from 0.1 to 1 MPa for a grain size of 10 mm (Karato *et al.* 1986). These stresses are close to the stresses induced in the mantle by GIA under Fennoscandia (Barnhoorn *et al.* 2011a) and the grain size is at the upper end of what is found for Fennoscandian mantle rocks (Kukkonen *et al.* 2003). Diffusion creep leads to a linear relation between stress and strain rate, whereas dislocation creep leads to power-law creep in which strain rate and hence viscosity depends non-linearly on stress.

Lateral variations in viscosity in GIA models have been studied (Sabadini *et al.* 1986; Wu *et al.* 1998, 2013; Martinec 2000; Wu & van der Wal 2003; Zhong *et al.* 2003; Latychev *et al.* 2005; Spada *et al.* 2006). Also the effect of power-law creep has been investigated separately (Wu 1992, 1999, 2001) and the combination of Newtonian and power-law creep has been implemented (Gasperini *et al.* 1992; Giunchi & Spada 2000). Such a combination, sometimes called composite rheology, has been shown to provide a significantly better fit to historic sea level data than purely linear and non-linear rheologies both in North America (Dal Forno *et al.* 2005; Dal Forno & Gasperini 2007) and globally (van der Wal *et al.* 2010). However, those studies assume that creep parameters are only varying with depth. The combination of lateral changes in temperature and power-law creep has been implemented in mantle convection models (e.g. Becker 2006) but not in models for GIA. In addition, no inferences have been made in terms of olivine deformation parameters such as grain size and water content and usually only a single set of upper-mantle temperatures has been considered in the above cited studies. Flow laws for the crust and shallow upper mantle were included in the finite element model of Schotman *et al.* (2009) but uncertainty in temperature variations and the combination of diffusion and dislocation creep were not included in that study and no GIA observations were used.

The rheology in van der Wal *et al.* (2010) contained a combination of diffusion and dislocation creep, and found that sea level data were better predicted with such a combination than with either flow law. Uplift rates of a composite rheology were increased relative to the low uplift rates that are generally found for purely dislocation (power-law) creep. Barnhoorn *et al.* (2011a) combined GIA induced stress with 3-D temperature variations underneath Fennoscandia, but did not explicitly model GIA thus it was not possible to compute uplift rates and sea level. Large variations in viscosity were obtained in Fennoscandia, and also viscosity variations with time were found due to the stress-dependence of effective viscosity for dislocation creep. Here we include a composite rheology with 3-D variations in temperature in a GIA model and confront the predictions with GIA observations.

GIA modelling requires knowledge of past ice thickness in addition to unknown mantle deformation parameters. The (global) ice loading histories that are employed in most GIA studies are implicitly based on mantle viscosity because they are constrained by the same GIA observations that are used to constrain the mantle viscosity (e.g. Lambeck *et al.* 1998; Peltier 2004). Exceptions are studies of GIA modelling in Iceland with ice models based on observations of glacier outlines and thinning rates during the last century (Árnadóttir *et al.* 2009) and GIA modelling in Fennoscandia (Lund *et al.* 2009) based on the model of Naslund (2006) which is only weakly dependent on mantle rheology.

Thus, GIA inversion results in a combination of ice thickness model and Earth rheology that best fits GIA observations. This combination is not necessarily a unique solution, or a solution that is in agreement with other physical constraints on the mantle rheology. The possible bias of ice models for mantle rheology is a drawback when investigating a new mantle rheology model. Here we use a recently developed ice model for our study area, Fennoscandia, (Stocchi *et al.* 2010) based on simple ice dynamics with observations of past ice margins and a proxy for the meltwater contribution of the total ice model. The model is independent from GIA observations and mantle rheology, which makes it suitable to provide constraints on upper-mantle deformation parameters.

Given the lateral variations in temperature observed by seismology and the possible contribution of power-law creep to the relaxation process, viscosities inferred from GIA studies represent an average over lateral extent, depth (depending on the size of the ice sheet), time and deformation mechanisms with different depth dependence (diffusion and dislocation creep). The averaging makes it difficult to compare GIA inferred viscosities to results from other studies of mantle rheology. Here we aim to see if GIA observations are in agreement with lateral variations in temperature inferred from seismic models and heatflow measurements, as well as experimentally derived flow laws for olivine. The study area is Fennoscandia where denser observations of GIA, Earth structure and ice extent exist than in other rebounding areas. Moreover, the GIA process there is particularly sensitive to the upper mantle (see Steffen & Wu (2011) for a review). Model predictions will be compared with relative sea level (RSL) observations and present-day uplift rate. We aim to answer the following questions:

(i) What are the parameters in the experimental flow law for olivine that are preferred by GIA observations?

(ii) Do the non-linear flow laws and upper-mantle temperature sets lead to a better fit with GIA observations than models based on linear flow laws or a 1-D viscosity profile?

We focus on the upper part of the mantle beneath Fennoscandia down to 400 km depth where olivine is believed to be the main mantle material. However, the Fennoscandian relaxation is also sensitive to deeper parts of the mantle (Peltier 1998), therefore variation in creep parameters below 400 km depth is also addressed.

The contributions of our study are the following:

(i) Parameters in olivine flow laws for diffusion and dislocation creep are constrained by GIA observations in the presence of lateral variations in temperature and for an ice model that does not assume prior rheology parametrization.

(ii) Four different approaches to obtain shallow upper-mantle temperatures are used.

The finite element model and input parameters needed for computing the solid Earth response is described in Section 2 and results are presented in Section 3. Effective viscosities resulting from the composite 3-D rheology are presented in Section 3.1. Comparison

with sea levels and present-day uplift rate takes place in Sections 3.2 and 3.3, followed by discussion and conclusions.

2 METHODOLOGY

The first subsection explains the constitutive equation used in the model and how it is implemented in the finite element model. The flow laws for olivine themselves are assumed known from laboratory experiments. However, some parameters are needed in the flow law to characterize the conditions in Fennoscandia, such as water content and grain size. Water content in the mantle underneath Fennoscandia is assumed unknown and grain size is loosely constrained based on xenoliths in Fennoscandia. Different temperature estimates for this study are obtained from other sources as is explained in Section 2.3. Finally, the ice model developed for this study is presented in the last subsection. Predictions of sea level curves and present-day uplift rate will be presented in Section 3 for the different parameters (grain size, water content, mantle temperature and ice model). The goal is to see if the 3-D composite rheology can match GIA observations and to determine what parameters give the best fit to those observations in order to improve knowledge of the rheology of the upper mantle beneath Fennoscandia.

2.1 Finite element model and mantle stress–strain rate relation

Olivine is the main mantle material, which controls deformation in the upper mantle. A general flow law for olivine aggregates is (Hirth & Kohlstedt 2003)

$$\dot{\varepsilon} = A\sigma^n d^{-p} f\mathrm{H_2O}^r \exp(\alpha\varphi) \exp\left(-\frac{E+PV}{RT}\right), \quad (1)$$

where A and α are constants, σ is differential stress, d is the grain size, $f\mathrm{H_2O}$ is water content, φ is melt fraction, E is activation energy, P is pressure, V is activation volume, R is the gas constant, T is absolute temperature, n, p and r are the stress, grain size and water fugacity exponents, respectively. There are two main deformation mechanisms, diffusion and dislocation creep (Turcotte & Schubert 2002). For each of those mechanisms eq. (1) holds, but with different parameters. Diffusion and dislocation creep can occur simultaneously, thus the contributions of both processes to the strain rate should be summed (Ranalli 1995, p. 326).

Following Wu (2004) we use a commercial finite element package, ABAQUS™. In ABAQUS the individual strain components are computed for a composite rheology as

$$\varepsilon = B_{\mathrm{diff}} q \Delta t + B_{\mathrm{disl}} q^n \Delta t, \quad (2)$$

where q is the von Mises stress $q = \sqrt{\frac{3}{2}\sigma'_{ij}\sigma'_{ij}}$ with σ'_{ij} an element of the deviatoric stress tensor. t is time, and B_{diff} and B_{disl} are creep parameters computed with eq. (1). This is equivalent to using the effective viscosity to calculate individual strain rate components (Ellis & Stöckhert 2004). The creep parameters B_{diff} and B_{disl} from eq. (2) are taken from the flow law of Hirth & Kohlstedt (2003), eq. (1)

$$B = Ad^{-p} f\mathrm{H_2O}^r \exp(\alpha\varphi) \exp\left(\frac{E+pV}{RT}\right). \quad (3)$$

In this equation p, r, A, E, V are assumed known and taken from Hirth & Kohlstedt (2003). Their values are summarized in Table 2. Melt in the mantle below Fennoscandia is not expected, therefore we have set $\alpha = 0$. In eq. (3) grain size, temperature, water content and melt fraction are assumed unknown or only loosely constrained; they are considered the free parameters in the model. From eq. (3) it is clear that the creep parameters B_{diff} and B_{disl} strongly depend on temperature, which in our model is varied for each element above 400 km depth. Due to their important control on strain rates upper-mantle temperatures are discussed in more detail in the following section.

In a power-law or composite rheology viscosity depends on stress. In order to show results in terms of mantle viscosity that can be compared with viscosity profiles in GIA studies the effective viscosities are presented in Section 3.1. The effective viscosity can be computed from the definition (e.g. Ranalli 1995):

$$\eta = \frac{\sigma'_{ij}}{2\dot{\varepsilon}_{ij}}, \quad (4)$$

in which $\dot{\varepsilon}_{ij}$ is an element of the strain rate tensor. Strain rate for parameters from uni-axial experiments (such as summarized by eq. 1) can be written using the Von Mises stress as (van der Wal 2009, appendix C)

$$\dot{\varepsilon}_{ij,\mathrm{disl}} = \frac{3}{2} B_{\mathrm{disl}} q^{n-1} \sigma'_{ij}; \quad \dot{\varepsilon}_{ij,\mathrm{disl}} = \frac{3}{2} B_{\mathrm{diff}} \sigma'_{ij}. \quad (5)$$

Adding the strain rate for both mechanisms to obtain the composite rheology yields

$$\dot{\varepsilon}_{ij} = \frac{3}{2} B_{\mathrm{diff}} \sigma'_{ij} + \frac{3}{2} B_{\mathrm{disl}} q^{n-1} \sigma'_{ij}. \quad (6)$$

Inserting in eq. (4) gives for the effective viscosity

$$\eta_{\mathrm{eff}} = \frac{1}{3B_{\mathrm{diff}} + 3B_{\mathrm{disl}} q^{n-1}}. \quad (7)$$

Note that eq. (4) of Barnhoorn *et al.* (2011a) has q in the first term in the denominator which should not be there. The effective viscosity is similar to Wu (1999, 2001) but shear experiments were assumed there and the equivalent deviatoric stress was used instead of the uni-axial equivalent (Von Mises) stress.

In the lithosphere a combination of dislocation creep and grain boundary sliding can occur, in which slip at a grain boundary is accommodated by dislocation motion. This type of flow law has stress exponent $n = 2$–3 and grain size exponent $p = 1$–2. This hybrid mechanism is not considered here because it is unlikely to occur in the asthenosphere (Hirth & Kohlstedt 2003).

Mantle material is assumed to be incompressible and the layering of elastic parameters is nearly the same as van der Wal *et al.* (2010) and Wu & Wang (2008), see Table 1. Boundaries between the layers are at the major seismic discontinuities at 400, 670, 1170 and 3480 km depth. In addition, because elastic parameters are not varied laterally, the boundary between lithosphere and asthenosphere is taken to be 120 km. Rigidity and density are obtained by volume averaging and a small amount of tuning to get more realistic density jumps at the layer boundaries. A model with more layers would result in larger computation time, which limits the number of rheologic parameters that can be investigated. Variation in elastic

Table 1. Elastic parameters for the earth model.

Layer	r (km)	ρ (kg m^{-3})	g_0 (m s^{-2})	μ ($\times 10^{11}$ Pa)	ν
Lith	6371	3196	9.79	1.81	0.50
UM	6251	3439	9.84	2.19	0.50
TZ	5971	3882	9.93	3.24	0.50
LM1	5701	4527	9.98	5.37	0.50
LM2	5200	5074	9.91	7.20	0.50
Core	3480	10925	10.63	0	0

parameters themselves could be a small source of uncertainty but it has been shown with the normal mode method that reducing the number of layers by volume averaging gives accurate results (Vermeersen & Sabadini 1997). Lateral variations in elastic parameters have been shown to have a negligible effect in elastic earth models (Mitrovica *et al.* 2011) and are not considered here.

The earth model is spherical with a $2^\circ \times 2^\circ$ grid spacing and self-gravitation is included using the iterative method of Wu (2004). Depth discretization is determined by the input temperature data as discussed in Section 2.3. Here we use the layers of Goes *et al.* (2000) which means element boundaries in the upper mantle are located at 35, 70, 120, 170, 230 and 400 km depth, which are used in Barnhoorn *et al.* (2011a) as well. The top 35 km forms the crust and is fully elastic. Below the crust each element in the upper mantle has different creep parameters (eq. 2) which, together with the stress, determine the effective viscosity as in eq. (7). For a large effective viscosity the element will not exhibit viscous flow on the time scale of glacial loading and it can be considered to be part of the lithosphere. Thus, geotherms and the thickness of the lithosphere are simulated by assigning each element between 35 and 400 km different creep parameters.

Typically, depending on the rheological parameters, a computation for one iteration requires a 2 d computation using parallel processing on a quad-core workstation. In order to be able to investigate a larger parameter space the number of iterations for the self-gravitation should be as small as possible. It was found that for a representative model, the maximum uplift rate changes by 8 per cent, going from zero to one iteration. From one to two iterations, the maximum uplift rate changes by 1 per cent. Based on this, the number of iterations is limited to two. The effect of the mesh size was investigated with a radially symmetric earth model with ice model ICE-5Gv1.2 and a six-layer approximation to earth model VM2. Between a $2^\circ \times 2^\circ$ grid and a $1^\circ \times 1^\circ$ grid the difference in uplift rate is 1.3 mm yr^{-1}, and the maximum difference in RSL at the Scandinavian sites used in this study is 12 m.

The size of the time increments Δt is selected automatically in ABAQUS based on the Creep Error Tolerance (CETOL) parameter calculated internally in the software as (ABAQUS Analysis User Manual) $(\dot{\varepsilon}_{t+\Delta t} - \dot{\varepsilon}_t)\,\Delta t$. This parameter should be set so that stresses are computed with sufficient accuracy which is achieved if the creep strain increment is much smaller than the elastic strain increment. We have verified for one of the models (the best-fitting model described in Section 3.2) that lowering the CETOL parameter, which leads to increased precision but longer computation time, does not change the results.

Following Wu (2004) the buoyancy force is implemented as Winkler foundation. Recently it was shown that the use of Winkler foundations in ABAQUS introduces a slight error if the boundary with density contrast is not flat but has a large slope because the direction of the force is perpendicular to the surface of the element instead of pointing in the radial direction (Schmidt *et al.* 2011), but this finding is not incorporated here because we have layer boundaries at constant depths and the slope of the deforming boundaries with a density contrast is small (about 1 part in 1000).

According to eq. (1) viscosity is determined by the total state of stress. Stress-induced changes in viscosity can affect the viscosity by two orders of magnitude, for wet rheology and a grain size of 10 mm (Barnhoorn *et al.* 2011a) if background stress is neglected. In the presence of a large background stress due to mantle convection the perturbation in stress due to GIA will have a smaller effect on the effective viscosity (Turcotte & Schubert 2002) which would make the inclusion of stress-dependence in the flow laws less important. However, from GIA studies it was shown that a background stress larger than 10 MPa would produce too small effective viscosities while the effect of background stress can be neglected if its magnitude is smaller than 1 MPa (Wu 2001). Tectonic stresses and GIA induced stresses in the mantle are likely to be of the same order of magnitude, 1–10 MPa (Ranalli 1995). Thus, inclusion of background stress is relevant. However, correct modelling of stress-dependence would require knowledge of the magnitude and the direction of background stress (Schmeling 1987) which is not available for the mantle. Therefore, the influence on background stress is not included in eq. (2). In the presence of a large tectonic stress, variations in the viscosity are expected with a magnitude equal to the stress exponent n of eq. (1) (Schmeling 1987). Such variations are small compared to uncertainties in viscosity from other parameters shown in Section 3.1, which are the focus of this study.

2.2 Flow law input parameters

Apart from dependence on stress, grain size, and temperature we focus on the difference of a dry and wet (saturated) rheology. The presence of water is known to have a weakening effect on rheology (Blacic 1972; Chopra & Paterson 1984) increasing strain rate in the upper mantle (Karato 2008, p. 189). Water content in the mantle can not be constrained easily, as seismic wave velocities are only weakly sensitive to water content and estimates for water content derived from electrical conductivity vary greatly (Karato 2011). Water content is simply varied between a dry ($r = 0$) and a wet stage ($r = 1$ and water content of 1000 H/10^6 Si) and grain size is varied in a range that agrees with grain sizes in kimberlites and peridotites (1–10 mm, Dijkstra *et al.* 2002; Kukkonen *et al.* 2003). Melt fraction is ignored in this study, as seismic and electrical conductivity results are consistent with relatively small melt fractions (Faul 2001; ten Grotenhuis *et al.* 2005). Moreover, melt is expected in warmer areas such as underneath Iceland (Barnhoorn *et al.* 2011b) but not in the relatively cold mantle beneath Fennoscandia. This study focuses on the rheology in the lithospheric mantle and shallow upper mantle. For the mantle below 400 km depth, strain rate is calculated according to eq. (2), but with $n = 3$. Creep parameters are fixed to those B_{disl} and B_{diff} from a composite, non-laterally varying, rheology model that have a good fit to global historic sea level data (van der Wal *et al.* 2010). This assumption is relaxed in Section 4 where it is investigated if fit to sea levels and uplift rate data can be improved by altering creep parameters below 400 km.

It is not necessary to specify where in the mantle diffusion and dislocation creep occurs, because strain rate for diffusion and dislocation creep is determined by material parameters that are either inserted in the models or computed within the model. The mechanism that has the largest strain rate will dominate the deformation. For high stress and large grain size dislocation creep dominates, but for low stress and small grain size diffusion creep dominates (see results in Barnhoorn *et al.* 2011a).

2.3 Upper-mantle temperatures above 400 km depth

Temperature in the upper mantle can be derived in different ways: from surface heatflow measurements and the diffusion equation, from seismic velocity anomalies, and from P–T diagrams derived from xenoliths. The uncertainties in the estimated temperatures are not well known, therefore we implement the first two approaches to obtain temperature maps with depth. Xenoliths are

only found in a few isolated places and it is not possible to produce a map of lateral temperature variations for a large area around Fennoscandia with this approach. Temperature can be estimated by more advanced methods than ours but only for a regional area. We implemented those as well, providing a total of four temperature sets (UMT1 to UMT4) that are discussed later.

2.3.1 *Surface heatflow (UMT1)*

Temperature can be derived from surface heatflow measurements using estimates for variation of thermal conductivity with depth and heat production in the crust (Chapman 1986). Artemieva & Mooney (2001) and Artemieva (2006) presented a global thermal model for the continental lithosphere based on borehole heatflow measurements, which is not used here because the oceanic lithosphere is not included. Instead we have employed the surface heatflow values produced by Shapiro & Ritzwoller (2004). With the aid of a shear wave velocity model they extrapolated a global set of surface heatflow values (Pollack *et al.* 1993) from different tectonic settings to areas of similar tectonic structure where there are no heatflow measurements.

Geotherms are computed using the equation for 1-D steady-state heat transfer for layers of constant heat generation and constant conductivity (Chapman 1986)

$$T_{i+1} = T_i + \frac{Q_i}{k_i}\Delta z_i - \frac{A_i}{2k_i}\Delta z_i^2, \tag{8}$$

$$Q_{i+1} = Q_i - A_i \Delta z_i, \tag{9}$$

where T_i is the temperature in the ith layer, Q is the heat flow; k is the thermal conductivity, A is the heat generation and z is the thickness of the layer.

Heat generation is taken to be 0.45 and 0.02 μW m^{-3} in the lower crust (15–35 km) and lithospheric mantle, respectively (Chapman 1986). Upper crustal heat production is calculated using an empirical relation that specifies that 40 per cent of the observed surface heatflow Q is attributed to upper crustal heat generation A_0 (Chapman 1986) as follows

$$A_0 = 0.4\left(\frac{Q}{D}\right), \tag{10}$$

with characteristic length of heat production D equal to 10 km (Ehlers 2005).

Thermal conductivity is 3.0 W m^{-1} K^{-1}. For computation, increments in layer thickness are 0.1 km, but the results are averaged over the layers used in the GIA model. When the temperatures cross the 1300°C mantle adiabat, the adiabat of 0.3°C per km is used (Turcotte & Schubert 2002). Temperature at 400 km depth turns out to be 1390°C (∼1660 K), which agrees with Ranalli (1995, p. 184) and with the olivine to spinel transition (Turcotte & Schubert 2002, p. 186).

Temperature maps at different depths below Scandinavia are shown in Fig. 1. The lateral variation derives from the variation in surface heat flow values Q. The parameters k and A in eqs (8) and (9) do not vary laterally. It can be seen that considerable lateral variations exist (more than 500°C), with hot areas in the west and cold temperatures in the east underneath most of the Scandinavian continent. Below 170 km there is very little lateral variation in temperature, because the temperature profiles are cut-off at the 1300°C adiabat. To check the temperatures obtained from our calculations they are compared with lithosphere temperatures underneath Fennoscandia from Artemieva (2006). Fig. 2 shows average temperature for the geographical area between 55° and 70° north and 5° and 35° east at the midpoint of the layers in the GIA model. Global upper-mantle geotherms from Turcotte & Schubert (2002) and Stacey & Davis (2008) are also shown. Despite the simplifications in our calculations and the difference in surface heatflows, there is reasonable agreement with the average temperatures beneath Fennoscandia derived from Artemieva (2006). Upper-mantle temperatures are somewhat lower than those of Artemieva (2006) at shallow depths, but higher at greater depths.

2.3.2 *Temperatures from LitMod3D (UMT2)*

A local, high-resolution temperature field was derived in a separate study by Gradmann *et al.* (submitted) for the region of Western Fennoscandia (56–71°N, 2–24°E, 0–400 km depth) with the software package LitMod3D (Fullea *et al.* 2009). Here, the heat flow equation is solved for a simplified 3-D subsurface model comprising the crust (conductive, high heat production), lithospheric mantle (conductive, low heat production) and sublithospheric mantle (convective, no heat production). The layer geometry is taken from published data sets (Calcagnile 1982; Artemieva 2006; Ebbing *et al.* 2012), with adjustments mainly applied to the depth of the lithosphere in order to match tomographic velocity constraints from the uppermost mantle (Medhus *et al.* 2009; Maupin 2011). Minor adjustments to the crustal structure additionally provide a good fit with the observed gravity field and isostatically compensated elevation. Crustal thermal properties are taken from previous studies from this region (Olesen *et al.* 2006; Slagstad *et al.* 2009; Kolstrup 2010). Thermal conductivities of lithospheric and sublithospheric mantle are pressure and temperature dependent, which provide for the self-consistency of the resulting, iteratively derived temperature field. Minor differences in the thermal conductivity of the western model domain (Norway) and eastern model domain (Sweden) result in a slightly enhanced temperature contrast across these regions. Boundary conditions define the temperatures at the top of the model, base of the lithosphere, and base of the model as 0, 1300 and 1520°C, respectively. The main characteristics of the temperature field UMT2 are a thinner, therefore hotter, lithosphere under southern Norway and a thicker, therefore colder, lithosphere under Sweden.

In the finite element model, the temperatures outside Western Fennoscandia are taken from the global temperature field UMT1. To avoid large steps in the temperature field that would show up as artificial patterns in the uplift rate, the mean difference between the LitMod3D temperatures and the UMT1 temperature at the boundary of the region is subtracted from the Litmod3D temperatures. After that a 200 km half width Gaussian filter is applied to smooth the temperature transition on both sides of the boundary. The resulting temperature maps in Fig. 1 show that the inclusion of regionally refined temperatures from LitMod3D lowers temperature values compared to UMT1.

2.3.3 *Temperature from global seismic velocity anomalies (UMT3)*

Mantle temperature can be derived from seismic velocity anomalies through a conversion of velocity anomalies to viscosity perturbations using scaling laws (Ivins & Sammis 1995). Such a conversion is used, for example, in Latychev *et al.* (2005) and Steffen *et al.* (2006). Compositional changes and pre-stress also contribute to seismic velocity anomalies (Ivins & Sammis 1995), but above 400 km the effect of composition is secondary to that of temperature (Cammarano *et al.* 2003). Wang *et al.* (2008) investigated different

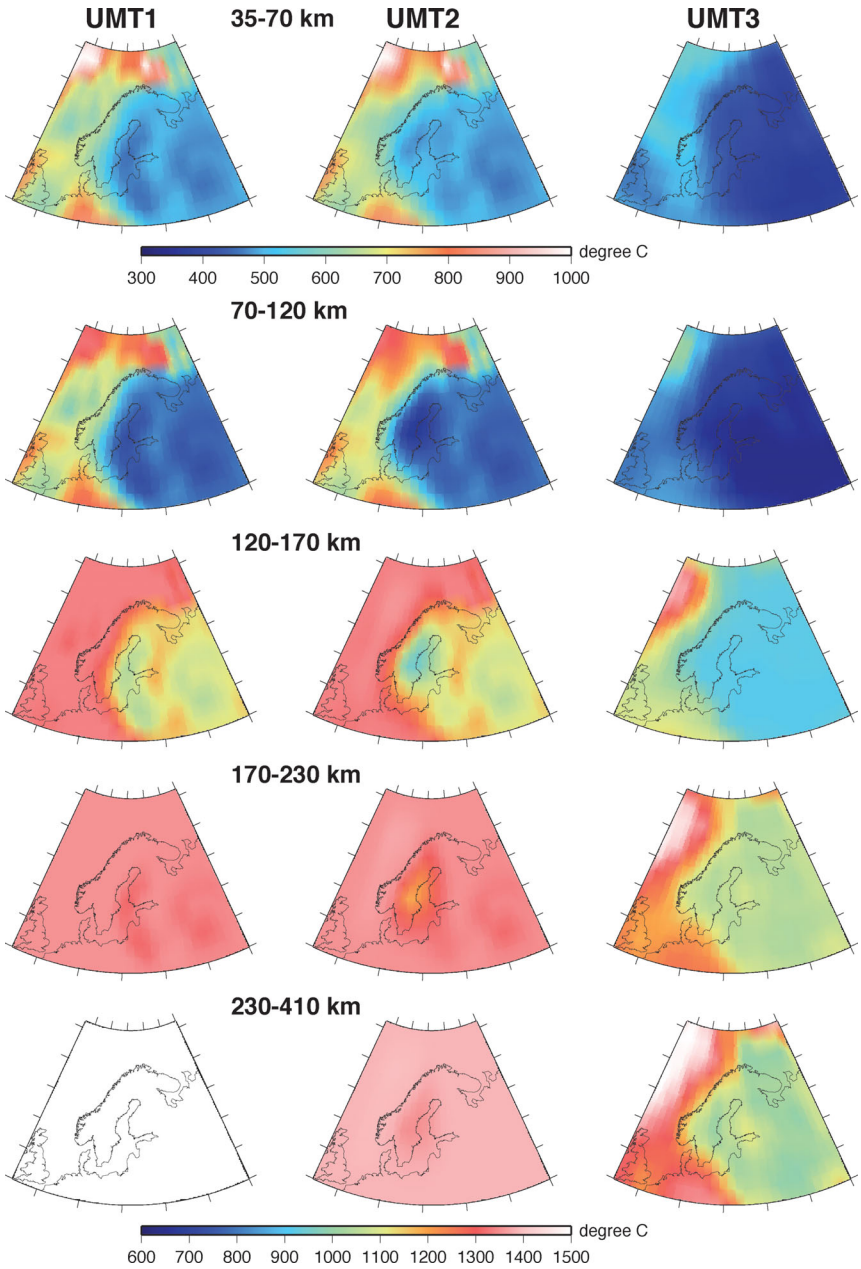

Figure 1. Temperature maps of the temperature sets UMT1, UMT2 and UMT3 at different depths. Note the different colour scales for the top layer and for the other layers.

gradations of thermal contribution (constant for the mantle) and found that a 20–40 per cent thermal origin explained most of the sea level data and present-day deformation rates. When including anelasticity and allowing the contribution to vary between upper and lower mantle, the thermal contribution rose to 60 per cent (Wu *et al.* 2013).

Seismic anomalies are given with respect to a reference seismic model that is itself an approximation of the real average seismic structure. As a result, absolute temperatures are not very well constrained from seismic measurements, see fig. 7 of Cammarano *et al.* (2003). Here we use an average of the upper-mantle continental and oceanic geotherms from Turcotte & Schubert (2002, p. 187) as background temperature. The variations with respect to this profile can be obtained from the temperature derivative of seismic wave velocities (Karato 2008)

$$\mathrm{d}T = \frac{\mathrm{d}\ln v_S}{\frac{\partial \ln v_S}{\partial T}} = \frac{\frac{\mathrm{d}v_S}{v_{S,0}}}{\frac{\partial \ln v_S}{\partial T}}, \tag{11}$$

where $\frac{\mathrm{d}v_S}{v_{S,0}}$ are the seismic wave velocity anomalies which are taken from the shear wave velocity model of Grand (2002). The values for the derivative with respect to temperature with depth are tabulated in Karato (2008, p. 376). For depths shallower than 80 km, the anelastic part of the temperature derivative is not given and we used the estimate that the anelastic effect is roughly equal to the

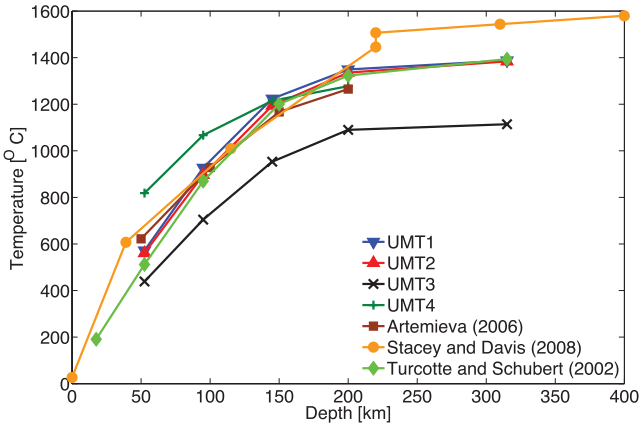

Figure 2. Averages of the temperatures maps used in the GIA modelling underneath Scandinavia compared to averages of the temperature maps from Artemieva (2006) and geotherms from Stacey & Davis (2008, p. 472) and Turcotte & Schubert (2002, p. 187).

anharmonic part (Karato 2008, p. 379). Note that in reality the correction for anelastic effects itself depends on temperature.

The global shear-wave velocity anomalies from Grand (2002) are interpolated to the midpoints of the layers in our model (52.5, 95, 145, 200 and 315 km depth) after which temperature anomalies are calculated according to eq. (11). From Fig. 1 it can be seen that the lateral variations in temperature computed in this way are smaller than the lateral variations in temperature derived from surface heatflow measurements (UMT1). However, at greater depths (below 170 km) the lateral variation is larger than for UMT1. In Fig. 2 it can be seen that the average UMT3 temperatures below Fennoscandia are lower than the UMT1 temperatures. The average seismic velocity anomalies underneath Fennoscandia are such that the average temperature is below the background geotherm from Turcotte & Schubert (2002) (Fig. 2) and the background geotherm itself is somewhat below the average of UMT1. Note that the both UMT1 and UMT3 use information from the oceanic and continental lithosphere: the surface heatflow data that is the basis for UMT1 contains measurements over the oceans, and the geotherm of Turcotte & Schubert (2002) is an average of oceanic and continental geotherms.

2.3.4 Temperature from seismic velocity anomalies (UMT4)

Temperature estimates derived for the upper 200 km of the Earth are available in Goes *et al.* (2000). In there, *P*- and *S*-wave seismic tomography data were inverted for temperature assuming a garnet lherzolitic composition of the upper mantle and using elastic and anelastic parameters from experimental data. Temperature estimate were produced at a resolution of $0.6^\circ \times 0.6^\circ$ in an area with longitudes from -35.6° to 60.4° and latitudes from 28.2° to 79.2° and depths of 35, 70, 120, 170 and 230 km. Outside and below the volume covered by the provided temperatures we use the composite rheology of van der Wal *et al.* (2010). Despite the boundaries of the Goes *et al.* (2000) area being far away from Fennoscandia the discontinuity between the creep parameters that are derived from the Goes *et al.* (2000) temperatures and the creep parameters from van der Wal *et al.* (2010) still produces unrealistic spatial patterns of uplift in Fennoscandia. Therefore UMT4 temperatures are not used in the sea level predictions, but only maximum uplift rates are investigated. It is expected that the latter are less dependent on the spatial pattern of relaxation. Temperatures from Goes *et al.* (2000) are larger than temperatures of Artemieva (2006) at shallower depths (see also Barnhoorn *et al.* 2011a, fig. 2). Since Artemieva (2006) is based on surface measurements, the temperature estimates therein are probably more accurate (uncertainty is estimated to be around 100°C) at shallower depths. The higher estimates in Goes *et al.* (2000) can be due to a variety of reasons, such as errors in the seismic model or the crustal model used in the inversion for velocity anomalies, or errors in the assumed composition of the mantle and experimentally derived elastic and anelastic parameters. They report an uncertainty of 100–150°C.

2.4 Creep parameters below 400 km depth

Below 400 km (or below 230 km for UMT4) creep parameters in eq. (2) are used that have a best fit to global sea level data in van der Wal *et al.* (2010). These are: $B_{\rm diff} = 1.1 \times 10^{-21}$ Pa^{-1} s^{-1}, which agrees with a Newtonian viscosity of 3×10^{21} Pa s, and $B_{\rm disl} = 3.3 \times 10^{-35}$ Pa^{-3} s^{-1} and $n = 3$. This means that lateral variation in effective viscosity can only arise if there are lateral variations in GIA induced stress. Stresses are larger close to the ice sheet, but fig. 1 of van der Wal *et al.* (2010) shows that stresses are such that dislocation creep is the dominant mechanism in a large region in the mantle.

Although the focus in this work is on the upper part of the upper mantle, it is investigated in Section 4 if modification in creep parameters below 400 km can improve fit with sea level and uplift data. There, $B_{\rm diff}$ is increased and reduced by a factor of three and $B_{\rm disl}$ is increased or reduced by a factor of ten.

2.5 Ice model

Since we are interested here in constraining the non-linear rheology of the mantle, it is necessary to employ an input forcing that is not biased by any a priori (linear) Earth rheology. Here we use a regional ice-sheet model for which the self-consistent variations of volume and thickness through time are computed by combining (i) continental ice-sheets volume variation which have been decoupled from deep-sea oxygen isotope records (Bintanja *et al.* 2005), (ii) reconstructed ice-sheet boundaries from surface glacio-geological sediment deposits (Ehlers & Gibbard 2003), and (iii) non-linear ice rheology and 1-D flow laws (Weertman 1961).

We employ the volume variation of the whole Eurasian ice-sheet aggregate which has been decoupled from the deep-sea δ^{18}O record using ocean temperature and Northern Hemisphere ice sheet models (Bintanja *et al.* 2005). We redistribute the ice mass over the time-varying Eurasian glaciated areas, which have been reconstructed by integrating and interpolating several surface glacial-geological indicators (full database from Ehlers & Gibbard 2003). These indicators consist of dated and calibrated end moraines and pro-glacial lake deposits which provide evidences of the position and migration of the ice-sheets margins through time.

At each time step (1000 yr long), we impose that the reconstructed ice-sheet margins accommodate the same ice volume as deduced from the δ^{18}O curve (Bintanja *et al.* 2005). For this purpose a perfect plastic ice rheology is chosen. Once the distance between the ice sheet margin and the ice divide is known, a parabolic profile can be built the size of which does not depend on the mass balance but only on the basal shear stress (Vialov 1958; Weertman 1961, 1974; Reeh 1982). A viscoplastic ice rheology was also considered but its effect on GIA observations was found to be small.

Our Eurasian ice-sheet chronology describes 21 kyr of melting during which ∼38 m of equivalent sea level (eustatic) were

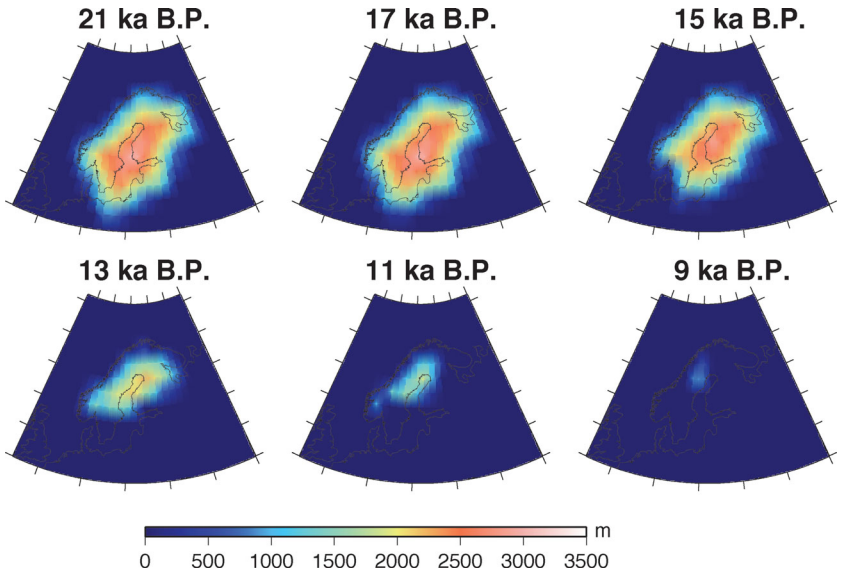

Figure 3. Ice thickness of the plastic ice model at six different time steps.

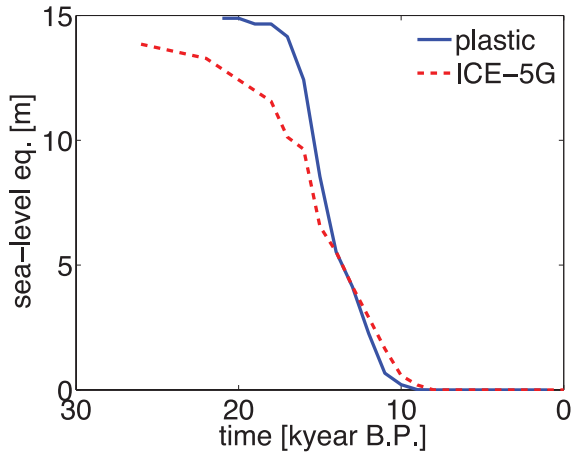

Figure 4. Ice volume expressed in equivalent sea level rise for the ice model used in this study and the Fennoscandian part of ICE-5G.

released to the oceans. However, for this work we only employ the Fennoscandian component as surface loading. To show the effect of uncertainty in the ice thickness variations we also present results for the ICE-5Gv1.2 model of Peltier (2004). Ice thickness is given at 0.7° horizontal resolution and interpolated to the 2° horizontal resolution used in our solid earth model. A linear loading phase of 90 000 yr precedes the melting starting at 21 000 yr. Ice thicknesses at 21, 17, 15, 12, 11 and 9 ka before present are shown in Fig. 3. In Fig. 4 the ice volume for the plastic ice model is compared to the volume of ice in the Fennoscandian part of ICE-5G. The maximum volume is larger in our ice model, and melt happens faster than in the ICE-5G model. The maximum ice height at the last glacial maximum is 3839 m, compared to 3219 m for ICE-5G and 2000 m for the RSES ice model (Lambeck *et al.* 1998). At 14 ka the maximum thickness is 3181 m, (2462 m for ICE-5G), and at 11 ka it is 2983 m (1607 m for ICE-5G). Thus, maximum ice thickness is quite different from widely used ice models, which are more tightly constrained by historic sea level data. However, it is important to note that the ICE-5G and RSES ice models are constrained to the sea level data by assuming a certain mantle viscosity that only varies with depth. Therefore, it is not possible to use those ice models to independently constrain mantle rheology. Our ice model is not based on assumptions about mantle viscosity, which allows us to investigate composite rheology and lateral variations in temperature. Also, larger ice thicknesses are required for producing realistic uplift rates for non-linear rheology (Wu 1999) and, to a lesser extent, for composite rheology (van der Wal *et al.* 2010).

A limitation of our ice model is that only the Fennoscandian component of the ice sheet is modelled so that it is not possible to compute global self-consistent sea levels. For comparisons to historic RSL observations in Fennoscandia we include melt water contributions of the other ice sheets that are computed a priori. In that a priori computation the volume of the other ice sheets is constrained by the same climatology as the Fennoscandian ice sheet. The sea levels are computed self-consistently for an ice sheet in North America and a linear mantle rheology with Newtonian viscosity of 3×10^{21} Pa s, which is equal to the linear rheology that is close to the best-fitting rheology in van der Wal *et al.* (2010). For Greenland and Antarctica only the melt water equivalent sea level change is included. These sea levels are added to the sea level contributions from the Fennoscandian ice sheet before comparison to RSL observations.

3 RESULTS

This section presents the model results. Section 3.1 shows viscosity profiles for a variation of model parameters and maps of effective viscosity for one model. After that, model predictions are compared to historic sea levels (Section 3.2) and GPS uplift rates (Section 3.3). The different data sets result in different best-fitting models. Therefore in Section 4 it is discussed whether variation in creep parameters below 400 km can produce a single model that fits all data sets.

3.1 Effective viscosity

Profiles of the effective viscosity (eq. 7) are plotted in Fig. 5. The width of each set of lines with the same colour shows the lateral

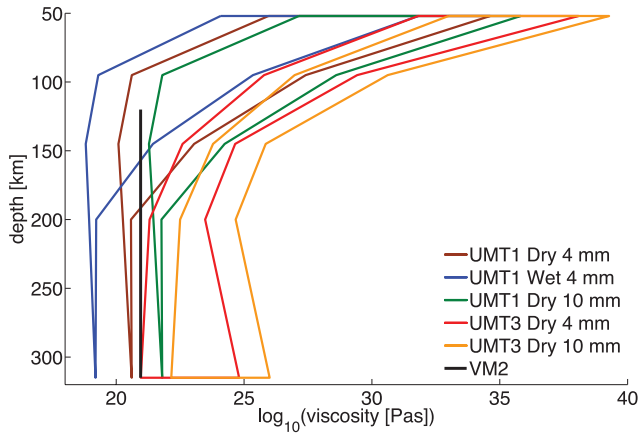

Figure 5. Depth profiles of viscosity below Fennoscandia for four different combinations of parameters. Each colour brackets the lateral variation in viscosity found in the region underneath the maximum ice extent according to our ice model.

variation in viscosity underneath the area in Fennoscandia that was covered with ice at the last glacial maximum according to our ice model. Viscosity decreases with depth down to 200 km, after which it levels off or slightly increases. The lateral variation for the UMT1 models is zero at depths of 315 km, reflecting the convergence of the UMT1 geotherms to 1390°C at 400 km depth. The UMT3 models result in larger viscosities, as expected from the temperature maps in Fig. 1. The spread in viscosities is smaller at shallow layers and larger at deeper layers, also consistent with the temperature maps. A grain size increase from 4 to 10 mm increases the viscosity for both UMT1 and UMT3, while the wet rheology lowers viscosities, here shown only for UMT1.

Maps of the effective viscosity are shown in Fig. 6 for a model which has a reasonable fit to uplift rates and sea level. Grey shaded areas have viscosity larger than 10^{25} Pas, for which viscous deformation was shown to be negligible over the glacial cycle (Barnhoorn *et al.* 2011a). Viscosity at a depth of 315 km is not shown because viscosity at that depth is nearly constant for UMT1, as can be seen in Figs 1 and 5. Although the GIA induced stress also influences the effective viscosity, the pattern in Fig. 6 resembles that of the UMT1 temperature maps in Fig. 1 such as the transition from cold to hot areas going from east to west, and patches of hot areas to the north and southwest of Fennoscandia.

3.2 Relative sea level

RSL data for sites from the Tushingham & Peltier (1991) database are used. Sites with less than four data points, or which span less than 4 ka, or which do not show a clear trend were removed, as well as some inconsistent sea level data points, which can not be fit by a smooth curve. The locations of the sites used here are shown in Fig. 7.

Comparisons with RSL data are usually performed in terms of chi-squared misfit (e.g. Wu 1999) defined as

$$\chi^2 = \frac{1}{N}\sum_{i=1}^{N}\left(\frac{o_i - p_i}{\sigma_i}\right)^2, \tag{12}$$

where N is the number of observations (183), o_i are the RSL observations, p_i are the predicted values from the models interpolated at the RSL locations and σ_i are the standard deviations corresponding to the RSL observations. However, the square in eq. (12) greatly

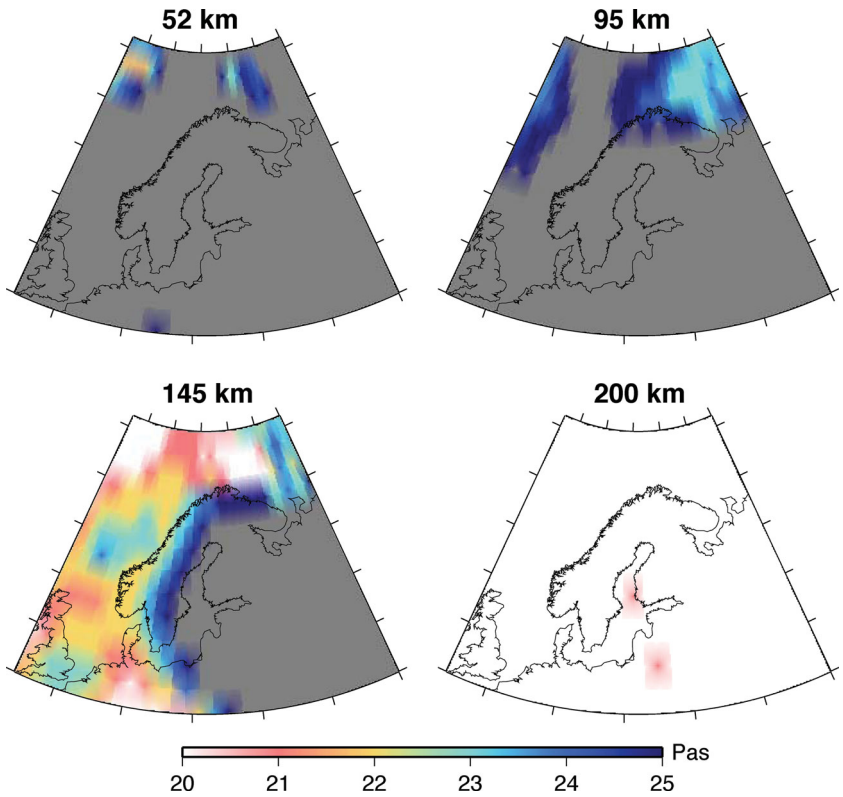

Figure 6. Effective viscosity for model UMT1 with dry rheology and 4-mm grain size at four different depths, calculated according to eq. (7). The grey shaded areas have viscosity larger than 10^{25} Pa s.

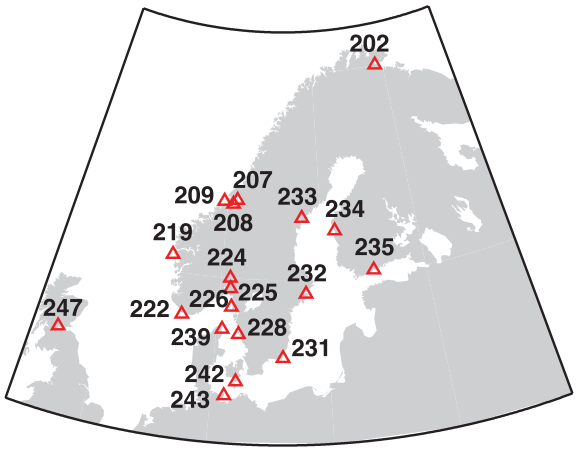

Figure 7. Location of the RSL sites from the Tushingham & Peltier (1991) database that are used in misfit analysis. The selection of sites is described in the text.

magnifies the misfit so that it can be dominated by the misfit of one or more data points. This is particularly true for 'outliers' resulting from the inaccuracies of the ice model and data points with small standard deviations. For example, the chi-squared misfit values are dominated by bad fits in E. Blekinge, Sweden (231). Therefore we prefer to use the one-norm misfit (e.g. Revets 2009), which is less sensitive to outliers and is defined as

$$\mu = \frac{1}{N}\sum_{i=1}^{N} \text{abs}\left(\frac{o_i - p_i}{\sigma_i}\right). \tag{13}$$

Both the one-norm misfit and the chi-squared misfit give the same best-fitting solution when data from site 231 is dropped. The one-norm misfit is shown in Fig. 8 for various rheological parameters and for the ice model of Section 2.5. For UMT3 in combination with a 1 mm grain size the viscosity is too low for stable computation within a reasonable computation time, therefore no results are shown for those parameters.

Several observations can be made in Fig. 8. First, there is a large difference in wet and dry rheology, demonstrating the large control that water content has on mantle rheology. Secondly, there is a considerable difference between dry UMT1 and UMT2 on one hand and dry UMT3 on the other hand, reflecting the differences

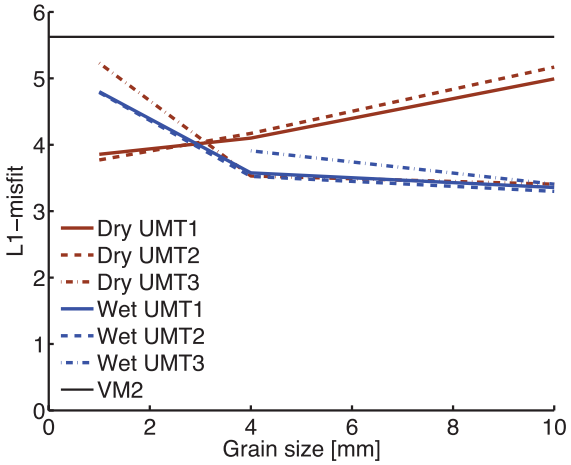

Figure 8. One-norm misfit for dry and wet upper-mantle rheologies for three different upper-mantle temperature sets and varying grain size, and for the VM2 profile. Ice model is the plastic ice model.

in viscosity profiles resulting from the different temperature sets (Fig. 5). Thirdly, wet rheology results in the smallest misfit, which agrees with the finding of Barnhoorn *et al.* (2011a) that a wet rheology results in acceptable viscosities. It is surprising that a stiff rheology such as UMT3/dry/10 mm leads to comparable misfit as the UMT1/wet/10 mm model. Possibly the large spread in viscosity for UMT3 models at depths below 200 km contributes favourably. For the UMT1 wet rheologies, the change in misfit from 4 to 10 mm grain size is small, indicating that the contribution of grain size dependent (diffusion) creep is small. Still, misfit generally decreases with increasing grain size. It can also be seen that the UMT2 model, which can be considered a local improvement of UMT1, results in a very small improvement in fit of the best-fitting dry and wet UMT1 models.

For comparison, Fig. 8 also contains the misfit for the widely used 1-D viscosity profile VM2 (Peltier 2004). We use Paulson *et al.* (2007)'s approximation of this profile in the finite element model: upper-mantle viscosity of 9×10^{20} Pa s, and lower-mantle viscosity of 3.6×10^{21} Pa s. The VM2 approximation performs worse than any of the models (wet versus dry and grain size). On one hand it might not be surprising that the addition of independent information in the form of flow laws and upper-mantle temperature leads to a better model. On the other hand, given the uncertainty involved in the flow laws and upper-mantle temperatures, it is encouraging that the extra information indeed improves the GIA model performance, as determined by sea level data in Fennoscandia. Since uncertainty exists in the ice history, it remains to be seen if the improved fit is also found for improved ice loading histories.

For upper-mantle temperatures derived from heatflow (UMT1/UMT2) and from seismic velocity anomalies (UMT3) the best-fitting rheology has a grain size of 10 mm. It appears from the curves that a better fit might be obtained with an even larger grain size. Such grain sizes are not observed in kimberlites in Fennoscandia (Kukkonen *et al.* 2003) but exposed peridotites in Norway contain remnants of centimetre-sized garnets, pyroxenes and olivines (Barnhoorn *et al.* 2011a). Sea level curves for the model with the best RSL misfit (UMT2, wet, 10 mm grain size) are shown in Fig. 9 together with the UMT3 model that has the best misfit (UMT3, wet, 10 mm grain size) and a model that is a compromise between small misfit and reasonable present-day uplift rate (UMT1, dry, 4 mm) as discussed in the next section. The curves match the observations well in some sites (202, 224, 226 and 232) but not so well in other sites (222, 228, 231, 235 and 239) which are in the south of Norway, Sweden and Finland (Fig. 7). It is possible that the coarse spatial resolution contributes to the bad fit. In the sea level codes, a $2^\circ \times 2^\circ$ surface element is either considered land or ocean. If the surface element is designated to be land in the model while in reality at that location the sea level observations are made on the coast, the water load is not considered correctly in the model. To take this into account the location where the sea level is computed can be shifted to better match the curves (Fig. 9, bottom row). Deviations still exist which can be due to local errors in the thickness of the ice sheet and the timing of melt. In particular, the large misfit in the south sites (228, 231, 242 and 243) means that our ice model is probably too thick in that region. Also the observations at site 247 in Scotland cannot be matched because the Scottish glaciation is not included in our ice model.

Widely used GIA models assume a linear relation between stress and strain in the mantle (e.g. Lambeck *et al.* 1998; Peltier 2004). Although these models ignore the presence of dislocation creep that is found in laboratory experiments, it is possible that GIA observations are fit well enough by such a simplified model. To test this, we

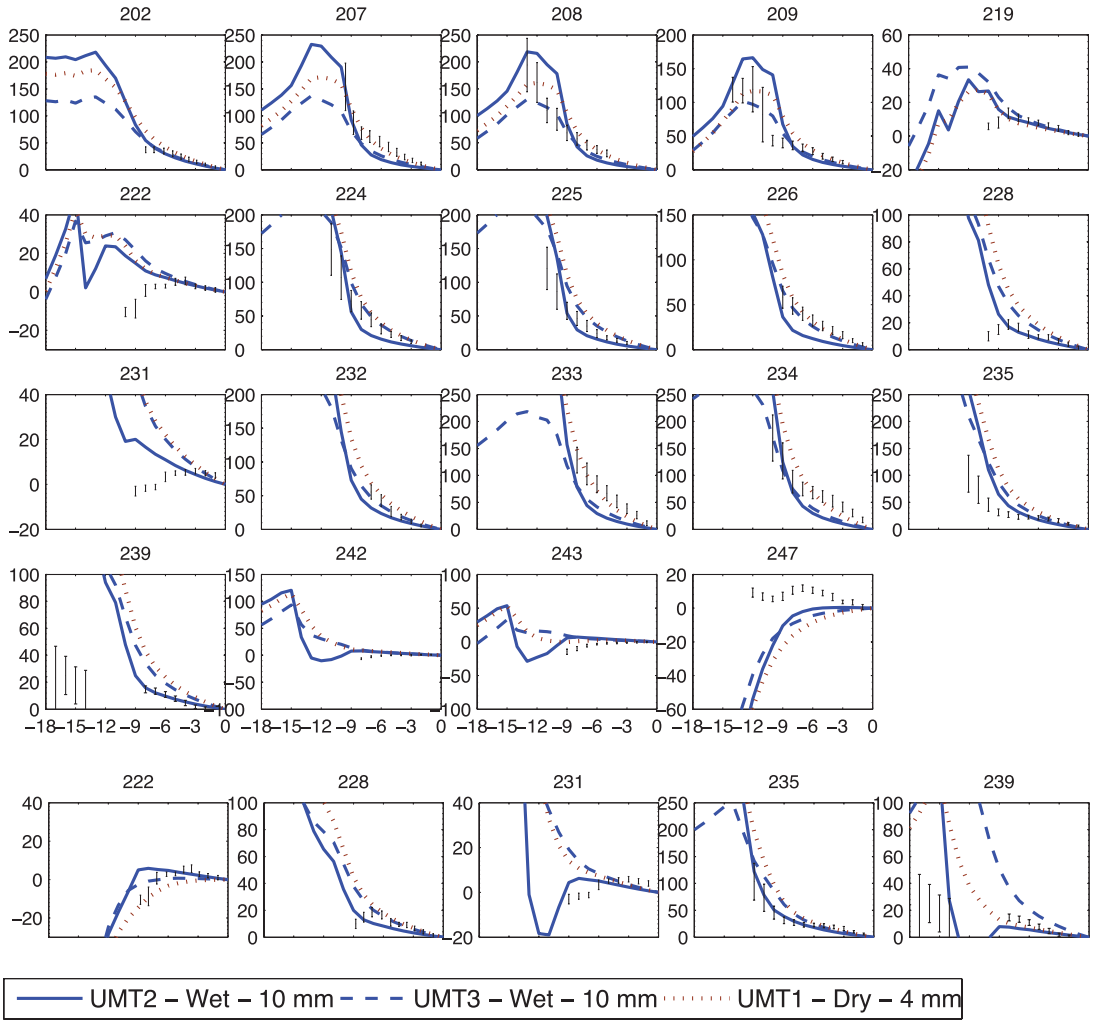

Figure 9. Relative sea level (RSL) curves for three different GIA models at the sites used in the misfit analysis: (i) the model that best-fitting sea level data (UMT2, wet, 10 mm), the UMT3 model with the best misfit (UMT3, wet, 10 mm grain size) and a model that is a compromise between small misfit and reasonable present-day uplift rate (UMT1, dry, 4 mm). RSL data are denoted by black lines with vertical length indicating the uncertainty in height. Bottom row: sea level curves for five sites with adjusted coordinates as described in the text. All coordinates are shifted 2° to the south, except 228 which is shifted 2° to the west.

show misfit for upper-mantle rheology with and without dislocation creep in Fig. 10. This partly answers the second research question on the importance of including non-linear flow laws. Because the presence of dislocation creep introduces variations in viscosity in space as well as in time, it is not straightforward to find a purely linear rheology that would be the best approximation of a composite 3-D rheology. Nevertheless, the figure shows that ignoring the dislocation creep leads to worse fit for large grain sizes. For small grain sizes the difference is insignificant because the contribution of diffusion creep is dominant in those cases. However, the best fit was obtained for a 10 mm grain size and wet rheology for which dislocation creep dominates (Barnhoorn *et al.* 2011a). These findings are still subject to uncertainty in the ice model but the improved fit of composite 3-D rheology relative to linear or power-law rheology separately is consistent with earlier studies on composite rheology (Dal Forno *et al.* 2005; Dal Forno & Gasperini 2007; van der Wal *et al.* 2010).

The uncertainty in the ice history is addressed in Fig. 11. There, misfit is compared between our ice model and ICE-5G. For ICE-5G the full model is used, and sea levels are computed self-consistently. This is an advantage compared to our model, where the sea level contribution from ice sheets outside Fennoscandia was calculated as described in Section 2.5. In Fig. 11 ICE-5G gives the smallest misfit for both temperature sets UMT1 and UMT3. This possibly reflects the tuning of the ice model to the sea level data of which the data used here is a subset. Fig. 11(a) also shows that based on ICE-5G the dry rheology fits better, while the plastic ice model shows the opposite. In addition, the dependence on grain size is different between the ice models. In general, fit improves for large grain size. This again suggests that grain sizes might be larger than expected.

Thus, there is a difference in the mantle rheology inferred from the plastic ice model and from ICE-5G, which could stem from inadequate modelling in our ice model, or from a bias in the ICE-5G model towards the viscosity profile that was used to create the model.

For a different mantle temperature set (UMT3) Fig. 11(b) shows that ICE-5G has a better fit for a wet rheology. This is because the lower temperatures of UMT3 underneath Fennoscandia by themselves lead to a higher viscosity than UMT1 (Fig. 6). In order to match sea level curves an additional lowering of the viscosity is required which can be achieved by a wet rheology. The misfit for

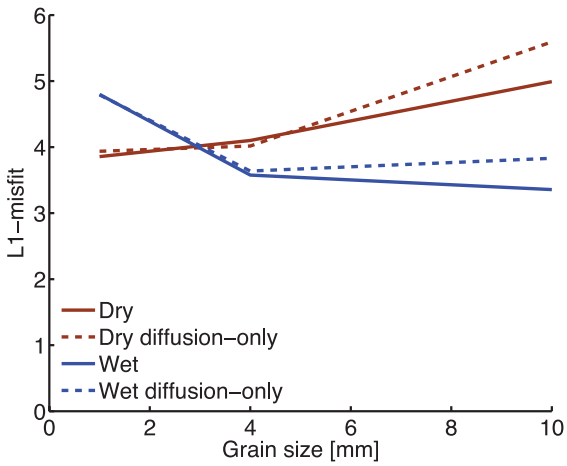

Figure 10. One-norm misfit for dry and wet rheology with and without dislocation creep for UMT1 (upper-mantle temperatures derived from heatflow) for the plastic ice model.

the VM2 approximation (viscosity varying in radial direction only) in combination with ICE-5G is also shown in the figure. The ICE-5G/VM2 model fits better than any of the composite 3-D rheologies with our ice model. However, much of that improvement comes from the ICE-5G model as opposed to the VM2 profile, because the misfits for models with lateral varying rheology in combination with ICE-5G achieve a comparable or even better fit than ICE-5G/VM2.

For a chi-squared misfit it can be tested whether the improvement in chi-squared fit is significant using an *F*-test (e.g. Dal Forno & Gasperini 2007) but for the one-norm misfit we are not aware of such a test. To be able to make a statement about the significant of the improvement in misfit, we calculate chi-squared residuals and perform an *F*-test assuming that the models are assumed to have three degrees of freedom (upper-mantle temperature data set, grain size and wet versus dry) compared to zero for ICE-5G/VM2. The chi-squared residuals show the same improvements in fit as the one-norm misfit shown in Figs 11(a) and (b), and the improvement is significant at 99 per cent confidence.

3.3 Uplift rate

It is known that purely non-linear rheologies result in too small present-day uplift rates (Wu 1999; Giunchi & Spada 2000). Uplift rates are somewhat increased when composite 3-D rheology is considered, which at the same time improves fit with sea level data (van der Wal *et al.* 2010). However, those results were obtained with existing global ice histories (e.g. ICE-3G, ICE-4G and ICE-5G) and with laterally homogeneous rheological parameters.

Fig. 12 shows maximum present-day uplift rates for the forward models, with heatflow derived temperatures (UMT1 and UMT2) in Fig. 12a and seismically derived temperatures (UMT3 UMT4) in Fig. 12b. Also results are shown for UMT1 and UMT3 in combination with ICE-5G. The maximum uplift rate observed in Fennoscandia is 10.1 mm yr^{-1} (Lidberg *et al.* 2007) shown as a shaded thick line in Fig. 12, the width of which shows the standard deviation in the observation. From Fig. 12a it can be seen that for all combinations of rheological parameters the predicted uplift rates are below the observed value. For a wet rheology uplift rates are much too small for all grain sizes, even for a different ice model (ICE-5G) and when dislocation creep is not considered (not shown). For UMT1 and UMT2 the uplift rates increase with increased grain size

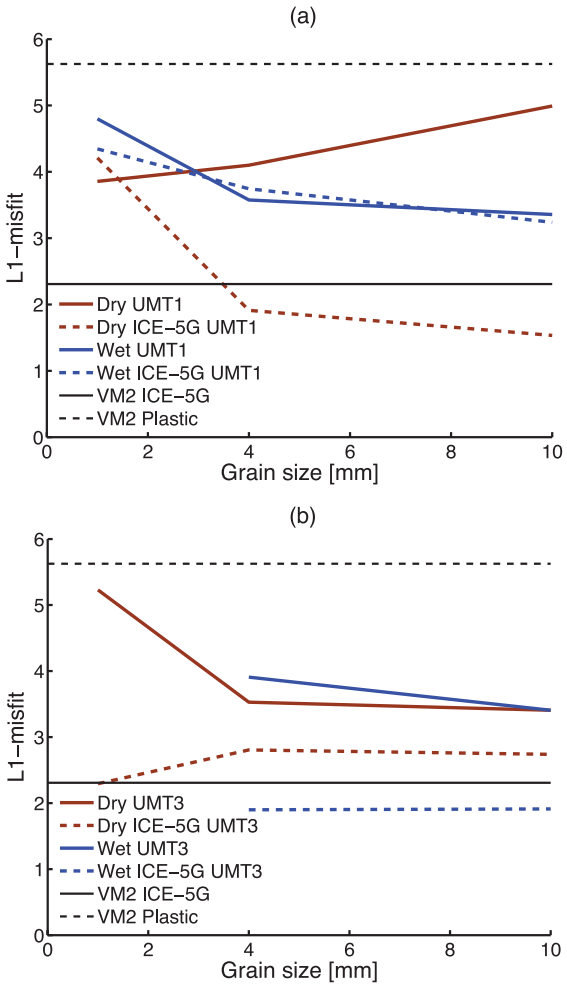

Figure 11. One-norm misfit for dry and wet rheology for the plastic ice model and ICE-5G. (a) UMT1 (upper-mantle temperatures derived from heatflow). (b) UMT3 (upper-mantle temperatures derived from seismic velocity anomalies).

(larger viscosity). For seismically derived temperatures (Fig. 12b) no conclusion for wet versus dry rheology can be made that is valid for all grain sizes and the increase in uplift rate with grain size observed for UMT1 and UMT2 also does not hold. An explanation for the good performance of UMT3/wet is that the low temperatures of UMT3 lead to a rheology that is too stiff, as noted in the discussion of Fig. 10, and uplift rates are increased if the viscosity is lowered by a wet rheology. Fig. 12(b) shows that for a dry rheology the uplift rate is reduced with grain size increase from 1 to 4 mm. Apparently, the relaxation is too slow and reducing the diffusion creep rate (thereby increasing effective viscosity) by increasing the grain size reduces the uplift rate. Similar to UMT1 and UMT2, the effect of a grain size increase from 4 to 10 mm is small.

For UMT4 the dry rheology also predicts larger uplift rates than the wet rheology, but the grain size dependence of the uplift rates is more difficult to understand. In Barnhoorn *et al.* (2011a) dislocation creep dominates at grain size of 10 mm and for a wet rheology at even smaller grain size. Also, dislocation creep is dominating the behaviour for the UMT4 temperatures, which are higher than the other temperature sets at depths up to 150 km (Fig. 2). The larger activation volumes for dislocation creep (Table 2) manifest in a larger temperature sensitivity of dislocation creep, which means that a larger part of the total creep is provided by dislocation creep which

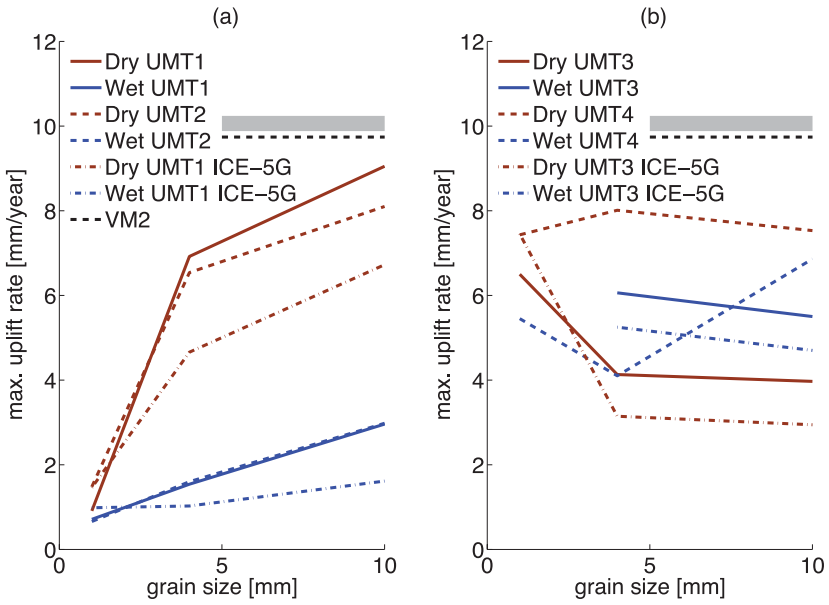

Figure 12. Maximum uplift rates for varying grain sizes. (a) UMT1 (plastic ice model and ICE-5G), UMT2, VM2 profile with plastic ice model. (b) UMT3 (plastic ice model and ICE-5G), UMT4 and VM2 profile with plastic ice model. The grey bar shows the observed maximum uplift rate of 10.1 mm yr^{-1} with 0.17 mm yr^{-1} error (Lidberg *et al.* 2007).

Table 2. Rheological parameters for dislocation and diffusion creep for a wet and dry rheology, from tables 1 and 2 of Hirth & Kohlstedt (2003).

	p	r	A	E (kJ mol^{-1})	V (m^3 mol^{-1})
Wet diffusion	3	1	1×10^6	335	4×10^{-6}
Dry diffusion	3	–	1.5×10^9	375	5×10^{-6}
Wet disclocation	1	1.2	90	480	11×10^{-6}
Dry dislocation	1	–	1.1×10^5	530	23×10^{-6}

is insensitive to grain size changes. This is at odds with the change in uplift rate for grain size increased from 4 to 10 mm. A possible explanation could be the large lateral variations in temperature in Goes *et al.* (2000), so that there are still areas dominated by diffusion creep at large grain size. The smaller area and depth of the for which UMT4 temperatures are available in comparison with UMT1–3 also makes interpretation difficult because much the regions outside and below the volume of UMT4 have much more influence on the relaxation underneath Fennoscandia.

It can be concluded that for all combinations of grain size and dry and wet rheology maximum uplift rates are too small. This is in contrast to the finding of Barnhoorn *et al.* (2011a) that wet rheology is necessary to find viscosity values in agreement with previous GIA studies. However, no dynamic simulations were performed there and in addition the averaging of effective viscosities in Barnhoorn *et al.* (2011a) over space and time does not necessarily correspond to the effective viscosity that is 'felt' by the GIA process. The question now is how can the GIA model be improved so that the uplift rates are in agreement with the measured uplift rate? Two solutions are briefly discussed: modifying the ice loading history, and ignoring dislocation creep. The uplift rates with the ICE-5G model are also presented in Fig. 12. Maximum uplift rates for this ice model are mostly below those with the plastic ice model, because the maximum ice thickness is smaller than for the plastic ice model. [An increase in maximum ice height has been shown to increase the uplift rate for a range of creep parameters (van der Wal *et al.* 2010, fig. 11)]. An exception is found for models with 1-mm grain size (UMT1/wet and UMT3/dry), which are conditions for which diffusion creep is enhanced and effective viscosity is low (Fig. 6). In that case, the larger ice heights of the plastic ice model also induce larger stress which increases the dislocation creep to the extent that relaxation proceeds too fast and remaining present-day uplift rates are lowered compared to the ICE-5G ice model. Using an ice model with viscoplastic ice rheology instead of plastic ice rheology only has a small effect on uplift rates. For UMT1 and a dry rheology with grain size of 4 mm, the maximum uplift rate decreases from 6.9 to 6.7 mm yr^{-1} (not shown), which is not significant considering the difference between modelled and measured uplift rates.

The second solution for increasing uplift rates is by modifying the creep parameters. It has been shown that creep with non-linear stress-dependence leads to small uplift rates (Wu 1999). Therefore, a purely linear rheology (i.e. ignoring dislocation creep) can bring the maximum uplift rate predicted with our model closer to the observed maximum uplift rate. However we found the difference to be small for a dry rheology. It is somewhat larger for a wet rheology but in that case uplift rates themselves are small and the observed uplift rates cannot be reached.

4 DISCUSSION AND CONCLUSIONS

Table 3 summarizes the fit of various combinations of parameters. For our ice model, the best fit to sea level data is found for a wet rhe-

Table 3. Overview of fit of models with respect to historic sea levels and present-day uplift rate.

		RSL (one-norm misfit)	Uplift rate (mm yr^{-1})
UMT1	Wet, 10 mm	3.4 (3rd best)	3.0 (too low)
	Dry, 4 mm	4.1	6.9 (OK)
	Dry, 10 mm	5.0	9.0
UMT2	Wet, 10 mm	3.3 (best)	3.0 (too low)
UMT3	Wet, 10 mm	3.4 (2nd best)	5.5 (low)
VM2		5.6	9.7

Table 4. One-norm misfit (bold) and maximum uplift rate in mm yr^{-1} (in brackets) for varying creep parameters below 400 km depth for the model with UMT1 dry rheology and 4 mm grain size.

Newtonian viscosity (Pa s)	$B_{\rm diff}$ (Pa^{-1} s^{-1})	$B_{\rm disl}$ (Pa^{-3} s^{-1})		
		$\mathbf{3 \times 10^{-34}}$	$\mathbf{3 \times 10^{-35}}$	$\mathbf{3 \times 10^{-36}}$
$\mathbf{1 \times 10^{21}}$	$\mathbf{3.3 \times 10^{-22}}$		**3.3** (4.4)	
$\mathbf{3 \times 10^{21}}$	$\mathbf{1.1 \times 10^{-22}}$	**2.8** (3.7)	**3.9** (6.9)	**6.5** (11.7)
$\mathbf{9 \times 10^{21}}$	$\mathbf{3.7 \times 10^{-22}}$		**3.9** (7.1)	

ology with 10-mm grain size, independent of the temperature data set. However, for this combination the maximum uplift rate is too low by 70 per cent for UMT1 and by 50 per cent for UMT3. For all upper-mantle temperature sets and grain size, reasonable uplift rates are only found for models with a dry rheology, while the best-fitting models to the RSL data are those with a wet rheology. Xenolith findings suggest a wet rheology in the asthenosphere (Kukkonen *et al.* 2003). Other constraints can come from geodynamic modelling. As example of this, dry olivine rheology has been inferred based on expected average radial viscosity profiles in a mantle flow model (Becker 2006), but a wet rheology was inferred based on predicted viscosities for a representative magnitude of GIA induced stress (Schotman *et al.* 2009; Barnhoorn *et al.* 2011a). Wet rheology was also shown to be required to obtain viscosity values close to the viscosities inferred from GIA studies (Barnhoorn *et al.* 2011a). Also, most of Fennoscandia is neither close to any active spreading ridge nor a subducting plate, thus the mantle below is more likely to be dry rather than wet (Dixon *et al.* 2004). We found a model with dry rheology, which has a sea level fit close to the best models (UMT3, dry, 10 mm), however, for that model the uplift rate is too small (3.9 mm yr^{-1}).

A grain size increase to 10 mm leads to a better fit to sea level data and larger uplift rate. This raises the question if indeed grain sizes are much larger in the upper mantle. Very large grain sizes (>50 mm) are observed in garnet peridotites in the western gneiss region in Norway (Barnhoorn *et al.* 2011a). We performed one computation with a grain size of 50 mm for the UMT1/dry model and found that uplift rate was reduced from 9.1 mm yr^{-1} at 10 mm grain size to 6.3 mm yr^{-1}, but L1 misfit was improved from 5.0 to 3.8. Thus simultaneous improvement of uplift rate and sea level data was not achieved even with very large grain size.

Sea level data and uplift rates prefer different models as discussed above. Therefore, the answer to the first research question on which flow parameters can be inferred from GIA observations, becomes a matter of how much value is given to the sea level misfit versus the difference between modelled and observed maximum uplift rate. RSL data are the most important GIA observable because they show the relaxation in time, while uplift rates are only a snapshot. From that perspective the fit to RSL data should be the more important constraint here. However, the differences in misfit in Fig. 8 are small, and the misfit can conceal variations in fit with location, see Fig. 9. The errors in the uplift rates can be estimated more accurately and the uplift rates are verified with other data sets such as gravity rates from GRACE (e.g. van der Wal *et al.* 2011). Here we considered only the maximum uplift rate irrespective of where it occurs. Therefore, the too small uplift rates for a wet rheology can be considered a more robust finding than the preference of RSL misfit for models with a wet rheology. The too low uplift rates could be due to be a problem in extrapolating the flow laws to mantle conditions. Errors in our temperature estimates are also a possible explanation, though the too low uplift rates are consistent for the temperature estimates that we produced. Uncertainty in the ice loading history is less likely, as the change in ice thickness or delay in melting required to achieve reasonable uplift rates is quite large (van der Wal *et al.* 2010).

A compromise between the sea level and uplift rate fit is found to be the model with heatflow derived temperatures (UMT1), dry rheology and 4 mm grain size. The sea level misfit for this model is below the average of all the models, and the uplift rate of 6.9 mm yr^{-1} is reasonably close to the observed value. Moreover, observed sea level curves near the centre of the ice sheet are approximated well by this model (Fig. 9) and it is for this model that viscosities are shown in Fig. 6. Sea level misfit shows a small preference for temperatures based on surface heatflow (Fig. 8), but this cannot be expected to be significant. The correct magnitude for uplift rates on the other hand can only be achieved with temperature fields based on surface heatflow data (UMT1 and UMT2, Fig. 12).

The fit to both data sets might also be improved by a change in the lower part of the upper- and lower-mantle parameters. Variations in creep parameters below 400 km depth certainly influence the relaxation as sensitivity kernels for Fennoscandia show nonzero values below this depth for radially symmetric earth models (e.g. Peltier 1998) and models with 3-D viscosity (Steffen *et al.* 2007). Below 400 km, we did not compute $B_{\rm disl}$ and $B_{\rm diff}$ with eq. (3) but selected the best-fitting ones from van der Wal *et al.* (2010). In Table 4 we vary those parameters and show the misfit and maximum uplift rate for the model in the second row of Table 3 (UMT1, dry, 4-mm grain size), which provides a reasonable fit to sea level data as well as the maximum uplift rate. It can be seen that a better fit for sea level data can be achieved by increasing the contribution of dislocation creep using a larger pre-exponent factor below 400 km depth, but then the maximum uplift rates are reduced. Maximum uplift rates can be slightly increased by a larger Newtonian viscosity in which case the RSL fit is similar. Alternatively, $B_{\rm disl}$ can be lowered below 400 km but this results in a worse RSL fit. Thus, a change in mantle parameters below 400 km does not improve the fit with sea level data or substantially increase uplift rates at the same time, and the cause for the discrepancy should be found elsewhere.

Uncertainties in the ice sheet model (spatial extent and timing of melt) limit the conclusions. Here we have used two very different ice sheet models. The true ice sheet thicknesses during the last glacial cycle might be outside the range captured by these two models and other ice models or improvements in the ice model might improve the fit to sea level data and uplift rate simultaneously. In this work we have opted for an ice model, which is not based on a mantle rheology and constrained by sea level data. However, it is very well possible that ICE-5G is a closer approximation of the true ice sheet geometry. Indeed, for the ICE-5G ice model the parameters that best fit to the RSL data are a dry rheology with 10 mm grain size in combination with UMT1 (Fig. 11). For this model the uplift rate is 6.7 mm yr^{-1}.

There are many parameters in the flow law for which more recent estimates exist, for example activation volume (Durham *et al.* 2009), which has a first order effect on effective viscosity (Karato & Wu 1993). However, it is not justified to replace one particular parameter from a more recent study into an existing flow law. Only by refitting more raw experimental data one could improve the flow law, but this is beyond the scope of this study. Instead we have accepted Hirth & Kohlstedt (2003) as being the most complete flow law for dislocation and diffusion creep, wet and dry conditions, for the same material. An alternative flow law (e.g. Korenaga & Karato 2008) is not taken into account in this study. We could have varied the parameters of the flow law within the uncertainty range specified in

Hirth & Kohlstedt (2003) but we have opted to test whether a single flow law matches GIA observations and focus on uncertainties in temperature, grain size and wet or dry state.

There are other sources of uncertainty in our modelling. Firstly, it is possible that olivine is not the weakest or dominating material in the upper part of the mantle. For example, it has been shown that under certain conditions, other minerals can result in lower viscosity than olivine (Barnhoorn *et al.* 2010; Skemer *et al.* 2010). Secondly, only diffusion and dislocation creep are modelled, while other deformation mechanisms exist, for example, grain boundary sliding. Thirdly, in our model grain size (and water content) are given one value for the upper mantle down to 400 km depth, but in reality grain size can vary with depth (Faul & Jackson 2005) and with location. Finally, the composition of the crust, not considered here, can also have a large effect on GIA observables (Schotman *et al.* 2009).

Despite the uncertainty, our study demonstrates that with input parameters from a variety of data sources (ice margin constraints, laboratory derived flow laws, seismology and heatflow measurements) can agree with sea level GIA observations in Fennoscandia. This contributes towards unifying mantle rheology across different disciplines. For our ice model the fit with sea level observations is better for 3-D models than for the VM2 profile, while for the ICE-5G model some 3-D models had a better fit than the ICE5G/VM2 model.

ACKNOWLEDGEMENTS

We are grateful to the reviewers for their effort and for helping us to improve the manuscript significantly. Hansheng Wang is thanked for providing us with the sea level solver for the finite element model. We thank Rob Govers and Irina Artemieva for comments. WW acknowledges funding from the ESF Eurocores programme TOPO-EUROPE, AB and WW acknowledge funding from the Netherlands Organization for Scientific Research (NWO). PW is supported by a Discovery Grant from NSERC (Canada).

REFERENCES

Árnadóttir, T., Lund, B., Jian, W., Geirsson, H., Björnsson, H., Einarsson, P. & Sigurdsson, T., 2009. Glacial rebound and plate spreading: results from the first countrywide GPS observations in Iceland, *Geophys. J. Int.,* **177,** 691–716.

Artemieva, I.M., 2006. Global $1^\circ \times 1^\circ$ thermal model TC1 for the continental lithosphere: implications for lithosphere secular evolution, *Tectonophysics,* **416,** 245–277.

Artemieva, I.M. & Mooney, W.D., 2001. Thermal thickness and evolution of Precambrian lithosphere: a global study, *J. geophys. Res.,* **106,** 16 387–16 414.

Barnhoorn, A., Drury, M.R. & van Roermund, H.L.M., 2010. Evidence for low viscosity garnet-rich layers in the upper mantle, *Earth planet. Sci. Lett.,* **289,** 54–67.

Barnhoorn, A., van der Wal, W., Vermeersen, B.L.A. & Drury, M.R., 2011a. Lateral, radial, and temporal variations in upper mantle viscosity and rheology under Scandinavia, *Geochem. Geophys. Geosyst.,* **12,** Q01007, doi:10.1029/2010GC003290.

Barnhoorn, A., van der Wal, W. & Drury, M.R., 2011b. Upper mantle viscosity and lithospheric thickness under Iceland, *J. Geodyn.,* **52,** 260–270.

Becker, T.W., 2006. On the effect of temperature and strain-rate dependent viscosity on global mantle flow, net rotation, and plate-driving forces, *Geophys. J. Int.,* **167,** 943–957.

Bintanja, R., van de Wal, R.S.W. & Oerlemans, J., 2005. Modelled atmospheric temperatures and global sea level over the past million years, *Nature,* **437,** doi:10.1038/nature03975.

Blacic, J.D., 1972. Effect of water on the experimental deformation of olivine, in *Flow and Fracture of Rocks,* Geophys. Monogr. Ser., Vol. 16, pp. 109–115, eds Heard, H.C., Borg, I.Y., Carter, N.L. & Raleigh, C.B., AGU, Washington, DC.

Calcagnile, G., 1982. The lithosphere-asthenosphere system in Fennoscandia, *Tectonophysics,* **90,** 19–35.

Cammarano, F., Goes, S., Vacher, P. & Giardini, D., 2003. Inferring upper-mantle temperatures from seismic velocities, *Phys. Earth planet. Inter.,* **138,** 197–222.

Chapman, D.S., 1986. Thermal gradients in the continental crust, *Geol. Soc., Lond., Spec. Publ.,* **24,** 63–70.

Chopra, P.N. & Paterson, M.S., 1984. The role of water in the deformation of dunite, *J. geophys. Res.,* **89,** 7861–7876.

Dal Forno, G. & Gasperini, P., 2007. Modelling of mantle postglacial relaxation in axisymmetric geometry with a composite rheology and a glacial load interpolated by adjusted spherical harmonics analysis, *Geophys. J. Int.,* **169,** 1301–1311.

Dal Forno, G., Gasperini, P. & Boschi, E., 2005. Linear or nonlinear rheology in the mantle: a 3D finite-element approach to postglacial rebound modelling, *J. Geodyn.,* **39,** 183–195.

Dijkstra, A.H., Drury, M.R. & Frijhof, R., 2002. Microstructures and lattice fabrics in the Hilti mantle section (Oman ophiolite): evidence for shear localization and melt weakening in the crust-mantle transition zone, *J. geophys. Res.,* **107,** doi:10.1029/2001JB000458.

Dixon, J.E., Dixon, T.H., Bell, D.R. & Malservisi, R., 2004. Lateral variation in upper mantle viscosity: role of water, *Earth planet. Sci. Lett.,* **222,** 451–467.

Durham, W.B., Mei, S., Kohlstedt, D.L., Wang, L. & Dixon, N.A., 2009. New measurements of activation volume in olivine under anhydrous conditions, *Phys. Earth planet. Inter.,* **172,** 67–73.

Ebbing, J., Olesen, O., England, R., Lauritsen, T., Stratford, W. & Weidle, C., 2012. Structure of the Scandes lithosphere from surface to depth, *Tectonophysics,* **536–537,** 1–24.

Ehlers, T.A., 2005. Crustal thermal processes and the interpretation of thermochronometer data, *Rev. Mineral. Geochem.,* **12**(58), 315–350.

Ehlers, J. & Gibbard, P.L, 2003. Extent and chronology of glaciations, *Quart. Sci. Rev.,* **22,** 1561–1568.

Ellis, S. & Stöckhert, B., 2004. Imposed strain localization in the lower crust on seismic timescales, *Earth Planets Space,* **56,** 1103–1109.

Faul, U.H., 2001. Melt retention and segregation beneath mid-ocean ridges, *Nature,* **410,** 920–923.

Faul, U.H. & Jackson, I., 2005. The seismological signature of temperature and grain size variations in the upper mantle, *Earth planet. Sci. Lett.,* **234,** 119–134.

Fullea, J., Afonso, J.C., Connolly, J.A.D, Fernandez, M., Garca-Castellanos, D. & Zeyen, H., 2009. LitMod3D: An interactive 3-D software to model the thermal, compositional, density, seismological, and rheological structure of the lithosphere and sublithospheric upper mantle, *Geochem. Geophys. Geosyst.,* **10**(8), doi:10.1029/2009GC002391.

Gasperini, P., Yuen, D. & Sabadini, R., 1992. Postglacial rebound with a non-Newtonian upper mantle and a Newtonian lower mantle rheology, *Geophys. Res. Lett.,* **19,** 1711–1714.

Giunchi, C. & Spada, G., 2000. Postglacial rebound in a non-Newtonian spherical Earth, *Geophys. Res. Lett.,* **27,** 2065–2068.

Goes, S., Govers, R. & Vacher, P., 2000. Shallow mantle temperatures under Europe from P and S wave tomography, *J. geophys. Res.,* **105**(B5), 11 153–11 169.

Goetze, C. & Kohlstedt, D.L., 1973. Laboratory study of dislocation climb and diffusion in olivine, *J. geophys. Res.,* **78,** 5961–5971.

Gradmann, S., Ebbing, J. & Fullea, J., submitted. Integrated geophysical modelling of a lateral transition zone in the lithospheric mantle under Norway and Sweden. *Geophys. J. Int.*

Grand, S.P., 2002. Mantle shear-wave tomography and the fate of subducted slabs, *Phil. Trans. R. Soc. Lond., A,* **360,** 2475–2491.

Ivins, E.R. & Sammis, C.G., 1995. On lateral viscosity contrast in the mantle and the rheology of low-frequency geodynamics, *Geophys. J. Int.,* **123,** 305–322.

Hirth, G. & Kohlstedt, D., 2003. Rheology of the Upper mantle and the mantle wedge: a view from the experimentalists, in *Inside the Subduction Factory, Geophysical Monograph Series,* Vol. 138, pp. 83–105, ed. Eiler, J., American Geophysical Union, Washington, DC.

Karato, S.-i., 2008. *Deformation of Earth Materials,* Cambridge University Press, Cambridge, UK, 463 pp.

Karato, S.-i., 2011. Water distribution across the mantle transition zone and its implications for global material circulation, *Earth planet. Sci. Lett.,* **301,** 413–423.

Karato, S.-i. & Wu, P., 1993. Rheology of the upper mantle: a synthesis, *Science,* **260,** 771–778.

Karato, S.-i., Paterson, M.S. & Fitzgerald, J.D., 1986. Rheology of synthetic olivine aggregates: influence of grain size and water, *J. geophys. Res.,* **91,** 8151–8176.

Kaufmann, G. & Lambeck, K, 2002. Glacial isostatic adjustment and the radial viscosity profile from inverse modelling, *J. geophys. Res.,* **107,** doi:10.1029/2001JB000941.

Kolstrup, M., 2010. The lithospheric mantle below southern Norway, *Master thesis,* University of Oslo, Oslo.

Korenaga, J. & Karato, S.-I., 2008. A new analysis of experimental data on olivine rheology, *J. geophys. Res.,* **113,** doi:10.1029/2007jb005100.

Kukkonen, I., Kinnunen, K. & Peltonen, P., 2003. Mantle xenoliths and thick lithosphere in the Fennoscandian Shield, *Phys. Chem. Earth,* **28,** 349–360.

Lambeck, K., Smither, C. & Johnston, P., 1998. Sea-level change, glacial rebound and mantle viscosity for northern Europe, *Geophys. J. Int.,* **134,** 102–144.

Latychev, K., Mitrovica, J.X., Tromp, J., Tamisiea, M.E., Komatitsch, D. & Christara, C.C., 2005. Glacial isostatic adjustment on 3-D Earth models: a finite-volume formulation, *Geophys. J. Int.,* **161,** 421–222.

Lidberg, M., Johansson, J.M., Scherneck, H.-G. & Davis, J.L., 2007. An improved and extended GPS-derived 3D velocity field of the glacial isostatic adjustment (GIA) in Fennoscandia, *J. Geod.,* **81,** 213–230.

Lund, B., Schmidt, P. & Hieronymus, C., 2009. Stress evolution and fault stability duringglaciation. TR-09–15, Svensk Karnbranslehantering AB.

Martinec, Z., 2000. Spectral-finite element approach to three-dimensional viscoelastic relaxation in a spherical Earth, *Geophys. J. Int.,* **142,** 117–141.

Maupin, V., 2011. Upper-mantle structure in southern Norway from beamforming of Rayleigh wave data presenting multipathing, *Geophys. J. Int.,* **185**(2), 985–1002.

Medhus, A., Balling, N., Jacobsen, B., Kind, R. & England, R., 2009. Deep structural differences in southwestern Scandinavia revealed by P-wave travel time residuals, *Norwegian J. Geol,* **89,** 203–214.

Mitrovica, J.X., Gomez, N., Morrow, E., Hay, C., Latychev, K. & Tamisiea, M.E., 2011. On the robustness of predictions of sea level fingerprints, *Geophys. J. Int.,* **187**(2), 729–742.

Naslund, J.-O., 2006. Ice sheet dynamics, in Climate and climate related issues for the safety assessment SR-Can. SKB TR-06–23, Svensk Karnbranslehantering AB.

Olesen, O. *et al.*, 2006. KONTIKI Report 2005–2006, Continental Crust and Heat Generation In: 3D. NGU Report 2006.059, 185p.

Paulson, A., Zhong, S. & Wahr, J., 2007. Inference of mantle viscosity from GRACE and relative sea level data, *Geophys. J. Int.,* **171,** 497–508.

Peltier, W.R., 1998. The inverse problem for mantle viscosity, *Inverse Problems,* **14,** 441–478.

Peltier, W.R., 2004. Global glacial isostasy and the surface of the ice-age Earth: the ICE-5G (VM2) model and grace, *Annu. Rev. Earth planet. Sci.,* **32,** 111–149.

Pollack, H.N., Hurter, S.J. & Johnson, J.R., 1993. Heat flow from the Earth's interior: analysis of the global data set, *Rev. Geophys.,* **31,** 267–280.

Ranalli, G., 1995. *Rheology of the Earth,* 2nd edn, Chapman and Hall, London.

Reeh, N., 1982. A plasticity approach to the steady-state shape of a three-dimensional ice sheet, *J. Glaciol.,* **28,** 431–455.

Revets, S.A., 2009. One-norm misfit statistics, *Geophys. Res. Lett.,* **36**(20), doi:10.1029/2009GL039808.

Sabadini, R., Yuen, D.A. & Portney, M., 1986. The effects of upper-mantle lateral heterogeneities on post-glacial rebound, *Geophys. Res. Lett.,* **13,** 337–340.

Schmeling, H., 1987. On the interaction between small- and large-scale convection and postglacial rebound flow in a power-law mantle, *Earth planet. Sci. Lett.,* **84,** 254–262.

Schmidt, P., Lund, B. & Hieronymus, C., 2011. Implementation of the glacial rebound prestress advection correction in general-purpose finite element analysis software: Springs versus foundations, *Comput. Geosci.,* **40,** 97–106.

Schotman, H.H.A., Vermeersen, L.L.A., Wu, P., Drury, M.R. & De Bresser, J.H.P., 2009. Constraints on shallow low-viscosity zones in Northern Europe from future GOCE gravity data, *Geophys. J. Int.,* **178,** 65–84.

Shapiro, N.M. & Ritzwoller, M.H., 2004. Inferring surface heat flux distributions guided by a global seismic model: particular application to Antarctica, *Earth planet. Sci. Lett.,* **223,** 213–224.

Skemer, P., Warren, J.M., Kelemen, P.B. & Hirth, G., 2010. Microstructural and rheological evolution of a mantle shear zone, *J. Petrol.,* **51,** 43–53.

Slagstad, T., Balling, N., Elvebakk, H., Midttomme, K., Olesen, O., Olsen, L. & Pascal, C., 2009. Heat-flow measurements in Late Palaeoproterozoic to Permian geological provinces in south and central Norway and a new heat-flow map of Fennoscandia and the Norwegian-Greenland Sea, *Tectonophysics,* **473,** 341–361.

Spada, G., Antonioli, A., Cianetti, S. & Giunchi, C., 2006. Glacial isostatic adjustment and relative sea level changes: the role of lithospheric and upper mantle heterogeneities in a 3D spherical Earth, *Geophys. J. Int.,* **165,** 692–702.

Stacey, F.D. & Davis, P.M., 2008. *Physics of the Earth,* 4th edn, Cambridge University Press, Cambridge, UK.

Steffen, H. & Wu, P., 2011. Glacial isostatic adjustment in Fennoscandia—a review of data and modeling, *J. Geodyn.,* **52**(3–4), 169–204.

Steffen, H., Kaufmann, G. & Wu, P., 2006. Three-dimensional finite-element modelling of the glacial isostatic adjustment in Fennoscandia, *Earth planet. Sci Lett.,* **250,** 358–375.

Steffen, H., Wu, P. & Kaufmann, G., 2007. Sensitivity of crustal velocities in Fennoscandia to radial and lateral viscosity variations in the mantle, *Earth planet. Sci. Lett.,* **257,** 474–485.

Stocchi, P., van der Wal, W., Vermeersen, L.L.A. & van de Wal, R.S.W., 2010. GIA simulation with plastic and visco-plastic ice models on a laterally heterogeneous 3D Earth model for Scandinavia, *Presented at 2010 Fall Meeting, Abstract GC41B-0812,* AGU, San Francisco, CA, 13–17 Dec.

ten Grotenhuis, S.M., Drury, M.R., Spiers, C.J. & Peach, C.J., 2005. Melt distribution in olivine rocks based on electrical conductivity measurements, *J. geophys. Res.,* **110,** B12201, doi:10.1029/2004JB003462.

Turcotte, D.L. & Schubert, G., 2002. *Geodynamics,* 2nd edn, Cambridge University Press, 456 pp.

Tushingham, A. & Peltier, W.R., 1991. ICE-3G: A new global model of late Pleistocene deglacation based upon geophysical predictions of postglacial relative sea level change, *J. Geophys. Res.,* **96,** 4497–4523.

van der Wal, W., 2009. Contributions of space gravimetry to postglacial rebound modeling with different rheologies, *PhD thesis,* Univ. of Calgary, Calgary, Alberta, Canada.

van der Wal, W., Wu, P., Wang, H. & Sideris, M.G., 2010. Sea levels and uplift rate from composite rheology in glacial isostatic adjustment modelling, *J. Geodyn.,* **50**(1), 38–48.

van der Wal, W., Kurtenbach, E., Kusche, J. & Vermeersen, L.L.A., 2011. Radial and tangential gravity rates from GRACE in areas of glacial isostatic adjustment, *Geophys. J. Int.,* **187,** 797–812.

Vermeersen, L.L.A. & Sabadini, R., 1997. A new class of stratified viscoelastic models by analytical techniques, *Geophys. J. Int.,* **129,** 531–570.

Vialov, S.S., 1958. Regularities of glacier shields movement and the theory of plastic viscous flow, *Int. Ass. Hydrol. Sci. Publ.,* **47,** 266–275.

Wang, H., Wu, P. & van der Wal, W., 2008. Using postglacial sea level, crustal velocities and gravity-rate-of-change to constrain the influence of thermal effects on mantle lateral heterogeneities, *J. Geodyn.,* **46,** 104–117.

Weertman, J., 1961. Stability of ice-age ice sheets, *J. geophys. Res.,* **66,** 3783–3792.

Weertman, J., 1974. Stability of the junction of an ice sheet and an ice shelf, *J. Glaciol.,* **13,** 3–11.

Wu, P., 1992. Deformation of an incompressible viscoelastic flat Earth with power-law creep: a finite element approach, *Geophys. J. Int.,* **108,** 35–51.

Wu, P., 1999. Modelling postglacial sea levels with power-law rheology and a realistic ice model in the absence of ambient tectonic stress, *Geophys. J. Int.,* **139,** 691–702.

Wu, P., 2001. Postglacial induced surface motion and gravity in Laurentia for uniform mantle with power-law rheology and ambient tectonic stress, *Earth planet. Sci. Lett.,* **186,** 427–435.

Wu, P., 2004. Using commercial finite element packages for the study of Earth deformations, sea levels and the state of stress, *Geophys. J. Int.,* **158,** 401–408.

Wu, P. & van der Wal, W., 2003. Postglacial sealevels on a spherical self-gravitation viscoelastic earth: effects of lateral viscosity variations in the upper mantle on the inference of viscosity contrasts in the lower mantle, *Earth planet. Sci. Lett.,* **211**(1–2), 57–68.

Wu, P. & Wang, H., 2008. Postglacial isostatic adjustment in a self-gravitating spherical Earth with power-law rheology, *J. Geodyn.,* **46,** 118–130.

Wu, P., Ni, Z. & Kaufmann, G., 1998. Postglacial rebound with lateral heterogeneities: from 2D to 3D modelling, in *Dynamics of the Ice Age Earth: A Modern Perspective,* pp. 557–582, ed. Wu, P., Trans Tech Publ., Switzerland.

Wu, P., Wang, H. & Steffen, H., 2013. The role of thermal effect on mantle seismic anomalies under Laurentia and Fennoscandia from observations of Glacial Isostatic Adjustment, *Geophys. J. Int.,* **192**(1), 7–17.

Zhong, S., Paulson, A. & Wahr, J., 2003. Three-dimensional finite-element modelling of Earth's viscoelastic deformation: effects of lateral variations in lithospheric thickness, *Geophys. J. Int.,* **155,** 679–695.